INSTITUTE OF PHYSICS PUBLISHING JOURNAL OF PHYSICS D: APPLIED PHYSICS

J. Phys. D: Appl. Phys. **36** (2003) R97–R126 PII: S0022-3727(03)34952-6

TOPICAL REVIEW

Elemental thin film depth profiles by ion beam analysis using simulated annealing—a new tool

C Jeynes[1], N P Barradas[2,6], P K Marriott[3], G Boudreault[1], M Jenkin[4], E Wendler[5] and R P Webb[1]

[1] University of Surrey Ion Beam Centre, Guildford, GU2 7XH, UK
[2] Instituto Tecnológico e Nuclear, E.N. 10, Sacavém, Portugal
[3] Department of Statistics, National University of Singapore, Singapore
[4] School of Electronics Computing and Mathematics, University of Surrey, Guildford, UK
[5] Friedrich-Schiller-Universität Jena, Institut für Festkörperphysik, Jena, Germany

Received 18 March 2002
Published 19 March 2003
Online at stacks.iop.org/JPhysD/36/R97

Abstract

Rutherford backscattering spectrometry (RBS) and related techniques have long been used to determine the elemental depth profiles in films a few nanometres to a few microns thick. However, although obtaining spectra is very easy, solving the inverse problem of extracting the depth profiles from the spectra is not possible analytically except for special cases. It is because these special cases include important classes of samples, and because skilled analysts are adept at extracting useful qualitative information from the data, that ion beam analysis is still an important technique.

We have recently solved this inverse problem using the simulated annealing algorithm. We have implemented the solution in the 'IBA DataFurnace' code, which has been developed into a very versatile and general new software tool that analysts can now use to rapidly extract quantitative accurate depth profiles from real samples on an industrial scale. We review the features, applicability and validation of this new code together with other approaches to handling IBA (ion beam analysis) data, with particular attention being given to determining both the absolute accuracy of the depth profiles and statistically accurate error estimates.

We include examples of analyses using RBS, non-Rutherford elastic scattering, elastic recoil detection and non-resonant nuclear reactions. High depth resolution and the use of multiple techniques simultaneously are both discussed. There is usually systematic ambiguity in IBA data and Butler's example of ambiguity (1990 *Nucl. Instrum. Methods* B **45** 160–5) is reanalysed. Analyses are shown: of evaporated, sputtered, oxidized, ion implanted, ion beam mixed and annealed materials; of semiconductors, optical and magnetic multilayers, superconductors, tribological films and metals; and of oxides on Si, mixed metal silicides, boron nitride, GaN, SiC, mixed metal oxides, YBCO and polymers.

1. Overview

We will review our recent software developments in thin film depth profiling with ion beam analysis (IBA, see the Glossary in section 2 for an explanation of the acronyms) in the context of the work of the community; discussing the scientific implications of these developments. We hope to show that these developments improve the usability of IBA to such an extent as to effectively establish a new depth profiling tool.

We start (section 2) with a simplified overview of IBA since we believe that our new software tool (the IBA

[6] Centre de Física Nuclear da Universidade de Lisboa, Avenida Prog. Gama Pinto 2, 1699 Lisboa Codex, Portugal

DataFurnace) will make IBA attractive to many users for the first time. The essence of this new tool is its solution of the 'inverse problem' of automatically extracting depth profiles from Rutherford backscattering (RBS) data: we therefore describe this inverse problem (section 3) and continue with an introduction to the simulated annealing algorithm on which the inverse problem's solution is built (section 4). This algorithm was first applied to RBS in 1997 by Barradas *et al*, and the mathematical analogy of 'annealing' is why we have called the code 'DataFurnace'.

After some RBS examples exemplifying the scope of the tool (section 5) we give details of the physics (the 'forward model') and the algorithm used (section 6). We have also included here some recent developments extending the code to moderately rough surfaces. Another problem is that we are forced by consideration of computation time to use a simple forward model involving only single scattering, and therefore multiple scattering effects cannot be fitted directly. However, we have demonstrated an effective method for accounting for this and related effects (section 7).

We describe and discuss the intrinsic ambiguity of IBA data and the systematic approaches to valid analysis in the presence of this ambiguity (section 8). We specifically revisit Butler's (1990) interesting example of ambiguity and show how DataFurnace is an excellent tool to explore valid interpretations of the data under a variety of constraints. We also show a number of examples using various forward recoil techniques.

It is one of the major benefits of this new tool that the determination of the confidence limits on the calculated depth profiles can be done as a natural extension of the algorithm. We discuss the precision that is available in this way (section 9). We also discuss the use of accurate calculations of energy resolution as a function of depth to enable us to do very high depth resolution analysis (section 10). Both of these features are used in the analysis of both SiGe multilayers analysed with RBS and deuterated polymer multilayers analysed with NRA (nuclear reaction analysis).

The accuracy of an analysis, discussed in section 11, is in the end the most important issue. The establishment of a new tool depends first of all on being able to demonstrate that the answers are correct. At last a routine analysis of non-trivial samples is available which is both complete and at state-of-the-art accuracy. Accuracy of analysis depends ultimately on the accuracy of the forward model: we end with a subtle discussion of limitations of the current forward model in the context of an extraordinarily precise analysis of an optical multilayer sample (section 12).

In conclusion, we point out possible future developments (section 13). The review is illustrated with a number of striking examples showing the wide range of samples that have been analysed using the whole range of the IBA depth profiling techniques. It is worth mentioning that DataFurnace is in increasing use by analysts for a variety of materials analyses and we briefly review this work here.

The Lisbon group have used high resolution RBS to monitor the fabrication of MnIr spin valves with nano-oxide layers formed from plasma oxidation of CoFe layers (Veloso *et al* 2000). This process is to enhance the magnetoresistance for magnetic memory application. Zhang *et al* (2001) have investigated processing problems with magnetic tunnel junctions (used for magnetic random access memory applications) fabricated with sophisticated metallic (and semi-metallic) multilayers and analysed with high resolution RBS. With Rossendorf they have profiled MBE GaN on Si (Alves *et al* 2002). The Rossendorf group has investigated nitriding of Al (Telbizova *et al* 2001a, b, Fitz and Möller 2002).

The group at Surrey has also: measured lateral stress in implanted gold films using a three crystal quartz resonator method and a detailed self-consistent RBS analysis (Way *et al* 1999); investigated surfactant behaviour in the formation of latex films (Tzitzinou *et al* 1999); characterized CVD deposited SiC on Si (Toal *et al* 1999) and sol–gel deposited Ta_2O_5 and TiO_2 dielectric films on silicon (Cappellani *et al* 1999); used complementary RBS and XPS to investigate tribological coatings (TiN, TiAlN and MoS_2 : Ti) on steel (Baker *et al* 2000); investigated low temperature growth of GaN (Young *et al* 2000); characterized amorphous iron dicilicide (Milosavljević *et al* 2001, 2002); and measured H and N content of a-C by Hi-ERD (Carey *et al* (2000, 2001): this work was done at Rossendorf and cited Barradas *et al* (2000a,b)).

The Cambridge group has characterized silicon anodically oxidized using a wave resonance plasma (WARP) source by RBS (Uchikoga *et al* 1999), and also characterized WARP deposited a-C : N : H films by He ERD/RBS (Rodil *et al* 2000). The Sussex group has profiled metal nanoparticles formed in glass by high dose implantation (Stepanov *et al* 1999, 2001a, b). Other British RBS applications include the characterization of gate oxides on SiGe MOSFETs (Riley *et al* (1999): Liverpool/London/Southampton); and the investigation of polycarbonate/polymethylmethacrylate interface chemistry (Hutchings *et al* 2001).

The Göttingen group has followed ion beam mixing of Si/C multilayers (Harbsmeier *et al* 2000) and Ta/Si bilayers (Bibic *et al* 2000, Dhar *et al* 2002) with RBS and other methods. They have also characterized cubic boron nitride (Zinin *et al* 2002), fluorinated amorphous carbon (Ronning *et al* 2001) and beta-iron disilicide (Wagner *et al* 2002). The Darmstadt group has investigated heavy ion induced metal–ceramic interface diffusion with RBS (Nagel and Balogh 1999, Nagel *et al* 1999). The Chinese group have followed the interdiffusion of superconducting heterostructures (PZT/YBCO) (Xie *et al* 1999).

2. Introduction to IBA

IBA is a cluster of techniques involving materials analysis by MeV ion beams. When an energetic ion strikes a target there are a variety of energy loss mechanisms, any (or all) of which can be used (together or separately) to obtain information about the target. Table 1 summarizes these techniques, and indicates those for which the IBA DataFurnace can be used to obtain elemental depth profiles. We emphasise that the IBA DataFurnace software we describe applies only to thin film composition depth profiling and not to the various microbeam imaging or channelling applications.

IBA is now a mature scientific technique, very widely used in electronic materials research, and throughout thin film science: the most useful single volume overviews are in the Handbooks (Mayer and Rimini 1977, Tesmer and Nastasi 1995). It is a very large and diverse field which we do not intend to

Table 1. Glossary of IBA techniques.

	Technique	Explanation	DataFurnace?
RBS	Rutherford backscattering	Nuclear Coulomb scattering, incident ion is detected ($Q = 0$)	Yes
EBS	Elastic (non-Rutherford) backscattering	Nuclear scattering as RBS, but where the Coulomb barrier is exceeded ($Q = 0$)	Yes
ERD	Elastic recoil detection	Synonym for FRS ($Q = 0$)	Yes
FRS	Forward recoil spectrometry	Synonym for ERD. As RBS (or EBS) but where recoiled target atom is detected. This has to be in a forward scattering direction for kinematical reasons	Yes
NRA	Nuclear reaction analysis	Non-elastic interaction ($Q \neq 0$). Resultant reaction product detected (usually proton, alpha or deuterium)	Yes
PIXE	Particle induced x-ray emission	X-rays from inelastic collisions of the incident ion with inner core electrons are easy to detect: similar spectra to EDAX	No
PIGE	Particle induced gamma ray emission	Special case of NRA, where a photon is detected	No
Channelling		Used with any IBA technique for quantifying and profiling damage in single crystal samples	No
Microbeam		The ion beam can be focussed and scanned and used as a scanning ion microscope. RBS and other spectra can be collected from specific regions of the sample. Usually used with PIXE	Yes
IL	Ionoluminescence	As PIXE, but lower energy photons detected	No
IBIC	Ion beam induced current	Microbeam technique for investigating semiconductor devices, which respond to single ion impacts	No
STIM	Scanning transmission ion microscopy	Detects energy loss of single ions penetrating (relatively) thick targets	No

review here, only making a few general comments that may be useful for readers not analysts themselves. These readers should note that practitioners will probably quibble with almost all of our generalizations here which are intended only to allow newcomers to grasp IBA in a concrete way.

The first of the international biennial IBA Conference series was held in 1973 (Mayer and Ziegler 1973): these are now very large meetings, IBA-14 (Möller *et al* 2000) had 362 participants and is supplemented by several other international conference series: both PIXE (see Malmqvist (1999)) and the microbeam (see Prozesky *et al* (1999)) have their own large conferences and there are many regional meetings. IBA is ubiquitous in the scientific thin film community: for example, IBA was used in 38% of the papers published at a recent IBMM (conference on the ion beam modification of materials: Vredenberg *et al* (1999)). And not only the materials community: for example, the Louvre Museum in Paris has its own dedicated accelerator (Amsel *et al* 1990), and there is extensive international application of IBA techniques to cultural and archaeological artefacts (see Respaldiza and Gómez-Camacho (1997)).

IBA uses incident beam energies ranging perhaps from 100 keV to 200 MeV. At the low energy end the detectors become very expensive, as do the accelerators at the high end: we will not attempt to summarize all the detectors and accelerators in use today. IBA really started when nuclear physics groups looked for new uses for their obsolete little 2 MV Van de Graaff accelerators in the 1960s and 1970s, and there are still some of these machines around. The typical machine being installed today is a 2 MV tandem machine which can deliver multiply charged beams up to perhaps 10 MeV.

An ion beam striking a solid target has many types of interaction, any of which can be used for analysis. We should point out that nothing prevents the analyst installing multiple detectors in the target chamber to detect any or all of these interactions simultaneously.

2.1. Photon emission

Ionoluminescence has the highest cross-section of all the interactions: this is a very young field (see, e.g. Bettiol *et al* (1994) and Yang *et al* (1994)). PIXE (Johanssen and Campbell 1988) typically uses a 3 MeV proton beam, although helium can also be used. It is directly comparable with electron probe microanalysis (EPMA) with very similar spectra, except that there is negligible primary bremsstrahlung background due to the much higher particle mass. PIXE therefore has much higher sensitivity than EPMA. Cross-sections can be hundreds of barns (1 barn $= 10^{-24}$ cm^2). However, it is hard to get depth profiles from PIXE spectra, and this technique is not yet implemented in DataFurnace although it is often a very useful complementary technique (see, e.g. Loh *et al* (1993)).

2.2. Elastic scattering

RBS (Chu *et al* 1978) typically uses a 2 MeV He beam with typical cross-sections of a barn: but for a similar energy proton beam the Coulomb barrier of light target nuclei (up to P) is exceeded and the cross-sections are no longer Rutherford. Where the interactions remain elastic we call the method EBS. EBS cross-sections can exceed RBS ones by orders of magnitude. Of course, two body interactions between the incident ion and the target nucleus will both scatter the ion and recoil the target nucleus into forward directions. The

recoils carry much information about the sample and can also be detected. This is known variously as FRS or ERD (Tirara *et al* 1996).

2.3. Nuclear reactions

Where the interaction energy is sufficiently high the nuclear structure becomes involved, the interaction may become inelastic, and nuclear reactions can occur: NRA is often very useful since it is isotope specific and there is often no background to the signal, but cross-sections typically fall by orders of magnitude (Vizkelethy 1995, Hirvonen 1995).

2.4. Imaging and channelling

Turning to beam and sample manipulation, microbeams as small as 50 nm have been formed, and 1 μm microbeams are in widespread routine use: thus lateral maps of the major, minor and trace elements of the sample are readily available by PIXE (see Watt and Grime (1987)). Note that for PIXE the excitation volume where the x-rays are generated is essentially determined by the beam spot size since protons are not deflected much by electrons. In contrast, the excitation volume for x-ray analysis in the SEM is determined by the electron beam energy, and is often larger than 5 μm across. Therefore, PIXE x-ray maps are typically of much higher lateral resolution than EPMA ones. Of course, secondary electron maps are of much lower resolution for PIXE than for the SEM.

High energy ion beams can be very well collimated and aligned with symmetry directions in single crystal samples, making lattice site and damage information available. Known as channelling, this is a very large field in its own right (see Feldman *et al* (1982), Götz and Gärtner (1988)).

Other interesting emerging fields include *in situ* observation of the electrical behaviour of working semiconductor devices by the ion beam induced current (IBIC: see, e.g. Breese *et al* (1998a)), and the characterization of the defect structure of thick crystalline samples using a channelled beam in transmission (STIM, see, e.g. Breese *et al* (1998b)).

3. The IBA inverse problem

3.1. Rutherford scattering

In 1911, Ernest Rutherford explained the structure of the atom as a positively charged nucleus surrounded by electrons, where the nucleus was tiny with respect to the size of the atom (already known then to be around 1 Å). He used a simple Coulomb potential and contradicted J.J. Thompson's 'pudding' model. Rutherford based his model on Geiger and Marsden's (1909) data on the 'diffuse scattering' (in backward directions) of alpha particles by metal foils, and Geiger's (1910) data on the most probable angle of scattering of transmitted particles. Although the most probable scattering angle is very low, indicating a distributed charge as in Thompson's model, backscattering events imply a concentrated charge at the centre of the atom (requiring the concept of the nucleus). Geiger and Marsden (1913) subsequently verified Rutherford's calculation of the scattering probability, or cross-section.

3.2. Elemental depth profiles

It turns out that simple silicon diodes very conveniently stop alphas of MeV energies, converting their energy into a cloud of electron–hole pairs which can be separated by the electric field if the diode is reverse biased. High quality electronics to determine the number of electrons arriving at the anode, and hence the energy of the particle, have been available for over three decades. These detectors are effectively 100% efficient, detecting every particle that strikes them. Thus, an alpha scattering experiment can determine the mass of the target nucleus (from the energy of the scattered alpha, using the kinematics: conservation of energy and momentum), the depth of the target nucleus (also from the energy of the scattered alpha, this time using the energy loss as a function of depth in the target material), and the concentration of the target nucleus (from the absolute number of scattered alphas, using the cross-sections that Rutherford calculated).

3.3. Mass-depth ambiguity

RBS spectrometry can therefore, in principle, determine the complete elemental depth profile of a sample from the energy spectrum of the scattered particles. However, the reader will have noticed that the scattered particle energy is a function both of the mass of the target nucleus, and of the depth of the target nucleus in the sample. This ambiguity in the interpretation of the detected particle energy is the origin of the inverse problem that is at the heart of this paper.

Brice (1973) has shown that the elastic backscattering spectrum has the form of a triple integral:

$$\Psi_e(E, E_3) = A\frac{\partial}{\partial E_3}\int_0^\infty \mathrm{d}x' \int_0^t N_e\,\mathrm{d}x \int_{E'}^{E} \mathrm{d}E_1\, P_{\mathrm{in}}\, P_{\mathrm{out}}\frac{\sigma(E_1)}{S(E_1)} \tag{1}$$

where Ψ_e is the number of incident particles energy E backscattered with energy E_3 into the detector from element e in the target. $N_e(t)$ is the number of scattering centres of element e at depth t in the target. For target atoms at the surface E_3 is given by the kinematical factor k_e: $E_3 = k_e E$, and in general $E'(E_3) = E_3/k_e$. E_1 is the beam energy before scattering for atom e at depth t in the sample. σ is the differential cross-section and $S = \mathrm{d}E/\mathrm{d}R$ where $\mathrm{d}R$ is the average distance travelled by an ion energy E while losing energy $\mathrm{d}E$. The pathlength into the target before scattering is given by x and the pathlength after scattering by x'. P_{in} and P_{out} are respectively the distributions in the projected range along the incoming and outgoing directions.

Of course, the measured spectrum is the sum of the Ψ_e for all the constituent elements of the target. There is usually no way to measure individual partial spectra Ψ_e.

3.4. Fitting by simulation

Clearly, to calculate the inverse $N(\Psi)$ is not easy analytically and we describe a new approach to this inverse problem below. The most widespread approach currently is a pragmatic application of trial and error. The standard treatment is to assume that the target has a certain structure, to calculate the spectrum that would be obtained from such a target, to

compare with the collected spectrum and then to iterate until a reasonable match is obtained. The skilled analyst, from long experience and cunning, recognizes certain features of the spectrum and will, usually quite quickly, converge to an acceptable solution.

This approach has a number of major drawbacks. First, it is entirely manual, requiring a skilled analyst to give each spectrum a treatment that can easily take hours. (It should be noted that many types of spectra can be treated faster, or require only limited data to be extracted. And of course, analysts have become adept at this.) Second, large numbers of samples cannot be handled where a full treatment is needed, since the analyst simply runs out of patience. Third, because of the difficulty of data analysis the temptation for the experimentalist is to make samples especially for the analysis, instead of analysing the samples that result from the experiment. Fourth, in cases where the experimenter has failed to keep the samples simple, the spectra can be complex so that the analyst has difficulty extracting definite depth profiles from the data: in these cases the analyst may remain uncertain of the validity of the result. Fifth, training these skilled analysts is difficult: they are almost invariably at least postgraduate student level. Sixth, we have developed the 'rule of thumb' (rough estimate), over many years of analysis, that to analyse reasonably simple data collected over one day requires three further days subsequent concentrated work by the analyst. Difficult data (or the inexperienced analyst) may take much longer! Clearly, to fully staff an accelerator will be very expensive. There are, currently, few labs offering a full commercial RBS service.

3.5. Fitting by simulated annealing

We have taken a completely different approach. At its heart is the simulated annealing algorithm, which is a global minimization algorithm using combinatorial optimization (see section 4). We have applied this algorithm to IBA data, yielding an algorithmic solution of the IBA inverse problem. Note that the manual procedure described above is not a true algorithm since it cannot be handled by a machine in the general case. The function of the analyst is now different: instead of trying to guess a rough structure that may be approximately consistent with the data, the analyst concentrates on specifying the machine calibrations, on specifying any prior knowledge of the sample, and on an appropriate metric for the validity of the result. For any given set of priors (these include instrumental parameters) the algorithm, not the analyst, will determine the depth profile. We should point out that the algorithm itself, as we have implemented it, has a large number of parameters which could be chosen by the analyst: our implementation has value largely because we have shown that we have found values of general validity for most of these parameters, and we give the analyst clear rules for the choice of the remainder.

We believe that the advent of this new algorithm will completely revolutionize the applicability of IBA techniques to thin film analysis since it addresses each of the six drawbacks enumerated above at a fundamental level. The improvements are so dramatic that we effectively have a new tool for thin film composition analysis.

4. Introduction to simulated annealing

In this section, we describe the various elements of the simulated annealing (SA) algorithm that lies at the heart of the IBA DataFurnace. This discussion is central to this paper.

The essential elements of the SA algorithm were invented 50 years ago by Metropolis *et al* (1953) with a group including Edward Teller, in the context of the discussion of the use of 'fast computing machines' and Monte Carlo methods to calculate the equilibrium value of any (thermodynamic) quantity using the canonical ensemble of statistical mechanics. They successfully calculated the equation of state for a two-dimensional ensemble with these methods using the Los Alamos MANIAC computer.

The fundamental SA theorem establishes that provided certain formal criteria are observed, the algorithm is guaranteed to find the absolute minimum of any piecewise continuous function. The implementation of the algorithm is always computationally relatively expensive, and a revival of interest in it followed the explosion of computing power in the 1980s. We have found the summary of Aarts and Korst (1989) useful. It has been used to solve previously intractable problems, known as 'NP-complete', that is 'non-deterministic polynomial time complete' where the computation time is not bounded by any power of the number of independent variables of the problem. Examples of these are: the travelling salesman problem (see Press *et al* (1992)), and the construction of automatic sentence parsers for natural language processing (see Wilks *et al* (1996)). It was actually in the context of the last application, serendipitously, that we came across SA. In fact, the NP-complete class of problems has provided an important stimulus for the development of SA, as Kirkpatrick *et al* (1983) point out in an interesting article that uses SA to solve the semiconductor chip layout design problem (as well as the travelling salesman problem).

4.1. The forward model

We will represent the elemental depth profile of a thin film as a sequence of layers of specified thickness, each containing certain elements in a given proportion. There are other ways of representing profiles, but this is quite general and is the natural representation for the calculation of the expected IBA energy spectra. Consider an arbitrary depth profile $\boldsymbol{x}$ which is a structure $\{l_i, \lambda_{ij}\}$, where the vector $\boldsymbol{l}$ is the list of layer thicknesses, and the matrix λ is the list of relative proportions of the elements for each layer (and hence $\sum_j \lambda_{ij} = 1$). Then the forward model is encapsulated in the function $\boldsymbol{F}(\boldsymbol{x})$ which calculates the energy spectrum $\mathbf{Y}(E)$ (cf equation (1)) expected for the sample with depth profile $\boldsymbol{x}$.

$$\begin{aligned} \mathbf{Y}(E) &= \boldsymbol{F}(\boldsymbol{x}) \\ \boldsymbol{F}(\boldsymbol{x}) &= \sum_e \boldsymbol{f}_e(\boldsymbol{x}) \end{aligned} \tag{2a}$$

where the forward model calculates a partial spectrum $\boldsymbol{f}_e$ for each chemical element in the sample, and the total spectrum is just the sum of the partials.

This forward model, which is discussed in detail later, is the essence of the calculation: without a forward model

the spectra cannot be interpreted. All existing simulation programs are essentially simply implementations of a forward model. We consider limitations of the existing forward model at the appropriate places.

4.2. The objective function

We have to have a way of comparing some profile $\boldsymbol{x}$ with the measured spectrum $\mathbf{Y}$. There are many possibilities, some of which we will discuss later. We could use the very simple and general χ^2 function to compare the measured n-channel spectrum $\mathbf{Y} = \{y_1, y_2, \ldots, y_n\}$ with the calculated one $\boldsymbol{F}(\boldsymbol{x}) = \{\psi_1, \psi_2, \ldots, \psi_n\}$, given by

$$\chi^2(\mathbf{Y}, \boldsymbol{x}) = \sum_i (y_i - \psi_i)^2. \tag{2b}$$

It is not necessary to use the χ^2 function, but some such function must be specified and this is known as the objective function $\mathrm{O}(\mathbf{Y}, \boldsymbol{x})$. To solve the inverse RBS problem the objective function has to be minimized. When $\mathrm{O}(\mathbf{Y}, \boldsymbol{x})$ is minimized an optimal solution $\boldsymbol{x}_\mathrm{o}$ has been found: $\mathrm{O}_{\min} = \mathrm{O}(\mathbf{Y}, \boldsymbol{x}_\mathrm{o})$. Note that there may be many indistinguishable solutions $\boldsymbol{x}_\mathrm{o}$. Normally we are content with any particular solution $\boldsymbol{x}$ that is near an optimal solution $\boldsymbol{x}_\mathrm{o}$, but we show later how to find both a most probable solution and also an estimate of the error of this solution.

4.3. Markov chains

SA depends on the mathematics of Markov chains (see Gilks and Richardson (1996)). These are simply sequences M_s of states s_i selected from a state space $\mathbf{S}$ such that $M_s = \{s_1, s_2, \ldots s_i, \ldots s_m\}$ where the s_{i+1}th entry in the chain depends only on the s_ith entry and not on any previous ones. More properly,

$$P(s_{i+1} \mid s_1, s_2, \ldots, s_i) = P(s_{i+1} \mid s_i) \tag{2c}$$

that is, the probability of s_{i+1} given s_i is independent of all states before i.

Then the Markov chain is constructed by the transition distribution $T(s_i) = s_{i+1}$. This distribution is composed of a generation distribution from which a proposed new state is generated, and an acceptance criterion which determines whether or not to accept this proposed state as the next entry in the Markov chain.

Barradas *et al* (1997) have pointed out that although $\mathbf{S}$ is extremely large, it is finite in principle because there are only 92 elements, and both sensitivity and energy resolution are finite. As an estimate, for any given beam and detection system

$$\log |\mathbf{S}| \approx \left(\frac{\prod_{i=1}^{e} 1}{\phi_i} \right) \log n \tag{2d}$$

where $|\mathbf{S}|$ is the number of states s in the space $\mathbf{S}$, there are e elements in the sample, ϕ_i is the relative sensitivity for element i and n is the number of separable layers. Note that typically no more than 50 layers can be distinguished ($n < 50$) and in each layer we can probably not determine the concentration of an element at better than 1% precision ($1/\phi_i < 100$). Therefore, the problem may be treated either as a discrete or (since $\mathbf{S}$ is so large) as a continuous problem, depending what is mathematically more convenient.

For SA the Markov chains are constructed in a particular way. The state space $\mathbf{S}$ is the space of all possible depth profiles $\boldsymbol{x}$. This is the same as the space of all conceivable samples. The Markov chains are then sequences of profiles $\{\boldsymbol{x}_1, \boldsymbol{x}_2, \ldots, \boldsymbol{x}_m\}$. The generation function for constructing $\boldsymbol{x}_{i+1}$ from $\boldsymbol{x}_i$ can be any method of selecting a new profile $\boldsymbol{x}$ from state space. It is the acceptance criterion that gives SA its remarkable properties.

4.4. The acceptance criterion

A proposed state $\boldsymbol{x}_p$ is accepted depending on how the objective function has changed from its value for the last element $\boldsymbol{x}_i$ of the current Markov chain under construction. We evaluate the change $\Delta = \mathrm{O}(\mathbf{Y}, \boldsymbol{x}_p) - \mathrm{O}(\mathbf{Y}, \boldsymbol{x}_i)$ in the objective function implied by moving from state $\boldsymbol{x}_i$ to $\boldsymbol{x}_p$, and if it is improving ($\Delta < 0$) we accept the state: $\boldsymbol{x}_{i+1} = \boldsymbol{x}_p$. However, if it is getting worse ($\Delta > 0$) we may also accept it according to the probability P given by the Metropolis criterion:

$$P \propto \exp - \left(\frac{\Delta}{T} \right) \tag{2e}$$

where T is a control parameter characteristic of the Markov chain under construction. It is not hard to recognize the similarity of this probability to the Boltzmann factor, with T analogous to temperature. Thus, for the construction of the Markov chains used in SA the Metropolis criterion (or some generalization of it) is used for the acceptance criterion: this gives the Markov chains a natural thermodynamic interpretation. If the Markov chains are long enough they will reach a 'thermodynamic equilibrium', that is, the expectation value of certain statistics will stabilize. The introduction of a probability into the transition function means that it can be viewed as a Monte Carlo process, and these Markov chain Monte Carlo (MCMC) techniques are currently of enormous mathematical interest (see, e.g. Gilks and Richardson (1996)).

4.5. The cooling schedule

The final component in SA is the cooling schedule. A sequence of Markov chains is constructed with steadily reducing 'temperature'. Then the SA theorem states that the objective function will be minimized provided that each Markov chain is long enough to have reached equilibrium, and provided that the cooling schedule is sufficiently slow.

4.6. Summary

SA is an algorithm for finding the global minimum of an objective function. The entire state space of this function is explored. A sequence of states (a Markov chain) is constructed in which succeeding states have an objective function that is either reducing or has a Boltzmann-like probability of increasing according to a parameter analogous to temperature. Hence the idea of 'annealing'. A sequence of Markov chains is then constructed with reducing temperature; the end point being an optimal solution. For IBA, the objective function for a proposed depth profile is constructed from the difference between the spectrum being fitted and that calculated with a forward model (a standard simulation code) from the proposed depth profile. Then the state space explored is the space of all possible depth profiles.

4.7. Algorithmic issues

The SA theorem proves that in the general case a global minimum in the objective function is reached in logarithmic time, that is, for Markov chain k the cooling schedule is given by a temperature sequence $T_k = T_0/\log(10 + k)$, provided that the initial temperature T_0 is sufficiently large (Geman and Geman 1984). Unfortunately, this implies ridiculously long computation times. In practical cases, geometrical cooling schedules are always used, that is $T_k = a^k T_0$, where typically in our case $a \sim \frac{1}{2}$. This implies that SA is efficient for some classes of problem, but may be very inefficient for others.

An interesting paper by Sorkin (1991) has given an indication of the circumstances in which SA can be expected to be efficient. He proves that for a state space with certain (rather artificial) fractal properties, a value of the objective function close to a global minimum can be found in geometrical time. But he shows that it is likely that a more general theorem for realistic fractal state spaces is also true. In a preliminary analysis of the state space for a representative RBS spectrum we have found that, in the vicinity of the global minimum and in certain representations (not the χ^2 one described above), the objective function has only one minimum (the global minimum). We therefore suspect that IBA spectra are likely to have quite well behaved objective functions which SA can solve easily. We will report on this in another place.

To demonstrate that our SA algorithm is well behaved we need to show that it converges properly. Barradas *et al* (1998e) have shown the variation of the average Si content of the last 50 elements (states $\boldsymbol{x}$) of each Markov chain in the cooling schedule at various depths for an annealed and oxidized iron silicide, plotted for the entire cooling schedule. In the substrate, the silicon content reaches its final value at a high temperature, but near the surface, where there are many more possible states due to the presence of lots of oxygen (with its small signal and consequent small influence on the χ^2), the final value is not reached until the end of the cooling. Marriott *et al* (1999) have also demonstrated that our MCMC algorithm is well behaved, in particular that it converges and 'mixes' properly. Mixing means that the sampling process explores all possible solutions in an efficient manner.

5. Mixed metal silicides

Our first set of examples is in the silicide system. One form of iron disilicide is a semiconductor, and in principle it should be possible to fabricate a heterojunction laser in silicon. On the other hand, cobalt disilicide is a metal, and interesting three-dimensional metallization schemes seem feasible. A successful fabrication method for thin films of either material in silicon wafers could have a dramatic impact on silicon processing for microelectronics. Ion beam synthesis of $\beta FeSi_2$ (using high dose ion implantation) has resulted in light emitting diode structures (Leong *et al* 1997), and the examples in this section are taken from related work.

5.1. Analytical solutions

Figure 1 shows a high dose, high energy Fe implant into Si such that the Fe and Si signals overlap. Depth profiles are not easy to extract from spectra like this even though in this case only two elements (Si and Fe) are involved. The SQUEAKIE code of Børgesen *et al* (1982) is a matrix inversion type of code which reconstructs the depth profile by a closed calculation from the separated partial spectra, also shown in figure 1. In this case, the partial spectra overlap and SQUEAKIE can be used iteratively, starting from the surface. Alkemade *et al* (1990) use the same type of iterative procedure. (There are other more general analytical approaches which we discuss below.)

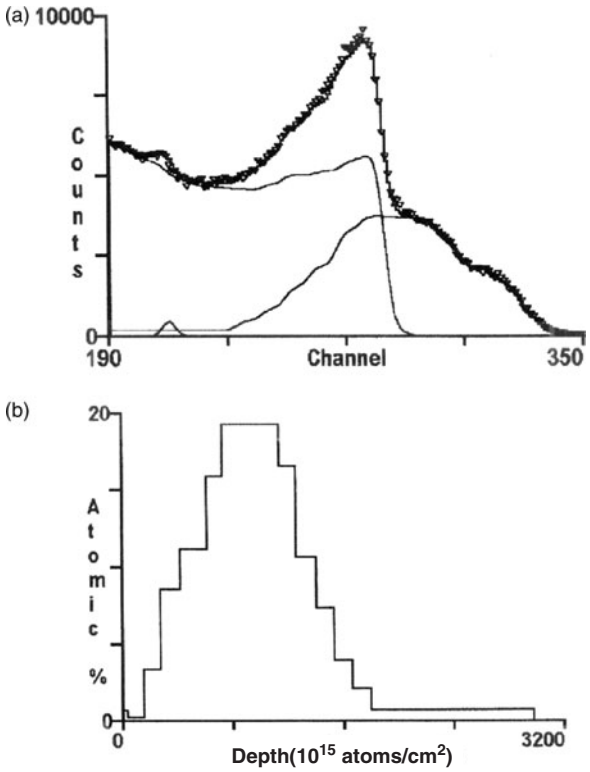

Figure 1. 1.5 MeV ^{3}He RBS of 200 keV 2×10^{17} Fe cm^{-2} implanted into Si. (*a*) RBS spectrum with fit (line through data points) and the Fe, Si and O partial fitted spectra (other lines). (*b*) fitted depth profile for Fe (after Belsen *et al* (1999)). Probably the Fe does not penetrate so deeply into the target (there is still apparently 'significant' Fe at 24×10^{17} atoms cm^{-2}): this is an ambiguity due to uncertainty in the charge collection. There is noticeable surface oxidation in this sample. Note on 'thin film units' (cf section 6, equation (3)): for silicon of density 2.32 g cc^{-1} or 5×10^{22} atoms cc^{-1}, one thin film unit (10^{15} atoms cm^{-2}) is 0.2 nm.

Figure 2 is a spectrum from a mixed Fe and Co silicide, and in this case with three elements we believe that no iterative procedure for SQUEAKIE exists. The kinematical gap between Fe and Co for these conditions is 18 keV, only slightly higher than the system energy resolution of about 15 keV (equivalent to about 30 nm of Si). Therefore, one would not expect there to be much discrimination between Fe and Co. The manual method using spectrum simulation described in section 3 above is tricky to use since it is not obvious how the contrast in the metal signal arises. Because of the difficulty and uncertainty of extracting the depth profile from the RBS spectrum, cross-sectional transmission electron microscopy, x-ray photoelectron spectroscopy and other techniques were deployed to determine the depth profile (Harry *et al* 1996).

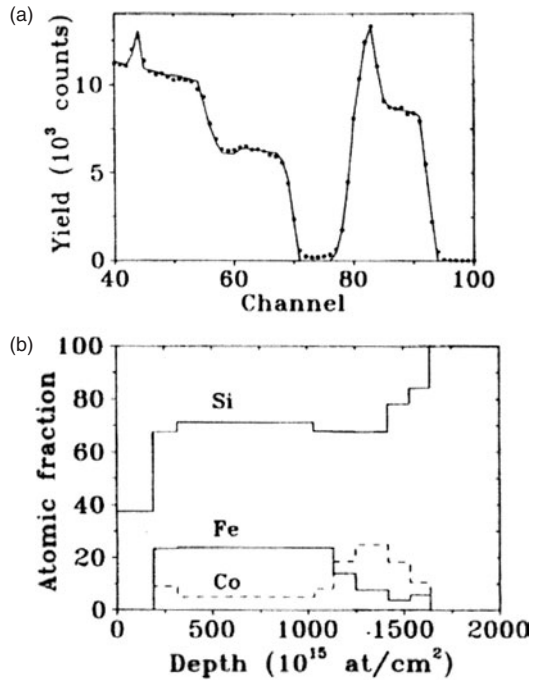

Figure 2. 1.5 MeV ^{4}He RBS of 200 keV 25×10^{16} cm^{-2} double implants of Co followed by Fe into Si. Implantation temperature was about 350°C. (*a*) RBS spectrum with fit (——) and Co and Fe partial fitted spectra (- - - -). (*b*) Fitted depth profile (figure 3 of Barradas *et al* (1997).) The surface is significantly oxidised, but the O profile is omitted for clarity. The depression in the Si concentration between about 10 and 15×10^{17} cm^{-2} corresponds to a cubic silicide, while below about 10×10^{17} cm^{-2} the layer has a stoichiometry similar to the Si-rich α-$FeSi_2$ phase.

5.2. Simulated annealing solution

It is because the spectrum of figure 2 is very contrasty, with many strong edges and peaks, that it is ideally suited to SA: even a rapidly prototyped SA code was able to find a solution very rapidly, taking only minutes on a 100 MHz 486 PC (Barradas *et al* 1997). This example was the first demonstration that SA was a powerful algorithm for solving the inverse RBS problem.

5.3. Sensitivity to collected charge

In Barradas *et al* (1998a) the data of Harry *et al* (1996) are re-analysed by SA, this time each fit taking about 2 min on a 200 MHz Pentium PC. The optimization of the cooling schedule is discussed, together with a demonstration that in this case, with contrast from barely separated masses, the Fe : Co ratio is extremely sensitive to errors in the charge collection. A 1% error in the charge gives a 20% error in the Fe content. Doubtless a careful analytical procedure might increase the precision of this type of measurement, but no-one has yet given a critical demonstration of charge collection better than 1%.

We will return repeatedly to the issue of instrumental parameters and the determination of analytical errors, here we emphasise that the collected charge is a critical parameter in the interpretation of IBA data. This is because for RBS spectra the cross-section is proportional to the square of the atomic number, so the absolute number of counts collected very strongly constrains the possible average Z (atomic number) of the sample. The same applies to all the IBA techniques since they all have strongly Z-dependent cross-sections.

With the manual method of spectrum simulation the charge is often treated as a free parameter (the analyst may simply 'normalize' the spectrum at an appropriate place). However, with the algorithmic approach of SA no tacit assumptions are allowed, and the explicit value given to the charge · solid-angle product is a very important constraint of the fitting process.

5.4. Batch analysis by simulated annealing

In Barradas *et al* (1998b) examples are shown of data from a set of over 50 samples investigating the kinetics of the ion beam mixing and annealing behaviour of sputtered metal films on silicon (figure 3). These spectra are also hard to analyse, especially since unwanted severe oxidation was experienced in the furnace annealing. By using SA, reliable quantitative data from this large set of hard spectra could be rapidly obtained, allowing useful conclusions to be drawn even in the presence of the oxidation (see also Milosavljević *et al* (2001, 2002)). With manual methods sufficiently precise results would not have been obtainable and the experiments would have had to be repeated.

Figure 3 shows a set of spectra (left-hand side) with the corresponding extracted depth profiles (right-hand side). The spectral plots show the data and the calculated fits (which go through almost all of the data points), and also the calculated partial spectra. The profiles (right-hand side) were obtained using a modified version of the matrix inversion code (SQUEAKIE) of Børgesen *et al* (1982) which can be applied directly since the partial spectra are available once the SA calculation is complete. The layer structure determined by SA is shown by the histogram lines in the top depth profile (figure 3(*a*), right-hand side).

5.5. Discontinuity of simulated annealing solutions

Figure 3 raises the interesting question of which representation is more fundamental, the discontinuous layer structure determined by SA, or the continuous profile determined by subsequently displaying the partial spectra calculated by SA as concentration versus depth, using SQUEAKIE? Clearly, the real depth profile is continuous, so experimentalists may prefer to see the inverted partial spectra rather than the raw layer structure. However, although SQUEAKIE has the advantage that the extracted depth profile uses all the spectral data in an (nominally) internally consistent way, the matrix inversion still has a number of problems.

First, the partial spectra are completely dependent on SA. Unavoidable statistical error in the estimation of the layer structure will cascade into the partial spectra and the profiles calculated from them. Moreover, the energy loss variation with depth used by the matrix inversion code is a function of the composition, where the layer structure is determined by SA. Therefore, the energy loss is an unavoidably discontinuous function of depth. Second, an iterative process of using the inverted profiles as the basis for a new proposed layer structure is not simple (and may be not possible) to implement since as the code stands the inverted profiles take

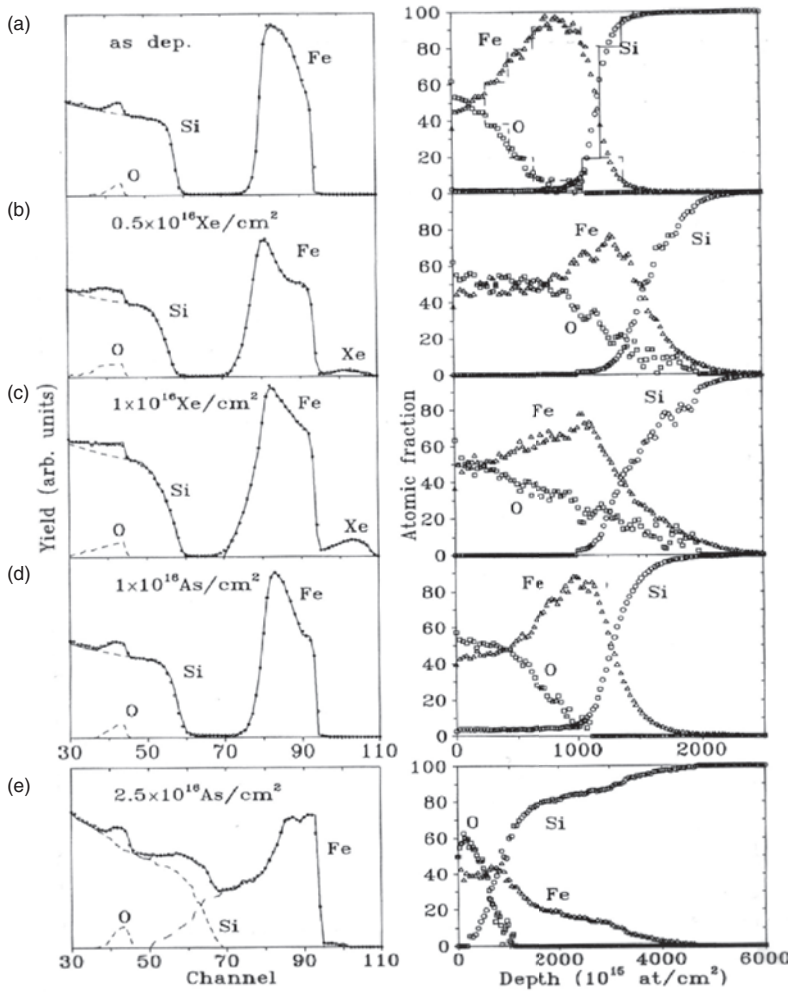

Figure 3. RBS data with simulated annealing fits (left), and corresponding derived depth profiles (right), of sputter deposited 120 nm Fe layers on Si ion beam mixed with either As or Xe and annealed at 900°C for 150 min. In the left column, the solid lines are the fitted spectra, and the partial O, Si and Fe spectra are shown as dashed lines. In the right-hand column the partial spectra extracted with DataFurnace are replotted as 'depth profiles' using SQUEAKIE (Børgesen *et al* 1982). For clarity, only one fitted depth profile is shown as a histogram (top spectrum, right-hand side column). Notice the different depth scale in the right-hand side column of *e*). Figure 2 of Barradas *et al* (1998b).

no account of the detector resolution or the variation of energy resolution with depth (energy straggling). In fact, Børgesen *et al* specifically point out that their algorithm will not handle energy straggling (or the surface signals) correctly. Third, the inversion necessarily assumes the accuracy of the forward model, but errors in the stopping power database (which can be at the 10% level as discussed in detail below) mean that the depths of interfaces may be inconsistently estimated between the different elements in the sample. We have seen very large artefacts demonstrably due to this effect.

We have therefore concluded that the layer structure determined by SA is the more fundamental, and for these and other reasons we no longer use the Børgesen matrix inversion code (SQUEAKIE). As we mentioned above, the apparent advantage of SQUEAKIE is that it nominally imposes self-consistency on the depth profiles obtained. But since we can demonstrate that actually these profiles are not internally consistent in general we are better off using a simpler inversion algorithm that does not claim self-consistency, treating each partial spectrum independently, while using a correct depth scale calculated from the fitted structure.

To summarize: we can replot the spectrum point by point on an elemental concentration versus depth scale, but this procedure is carried out on each partial spectrum independently without attempting to force self-consistency between the various replotted partial spectra. It is done only after SA determines a valid structure (depth profile) for the sample, and using the depth dependent energy loss calculated from this structure. The plots obtained take no account of energy resolution and straggling, but they are very useful in some circumstances.

5.6. Occam's Razor

We have up to now invoked the principle of Occam's Razor (*non sunt multiplicanda entia praeter necessitatem*, that is, entities are not to be multiplied except of necessity; in other words, 'minimize your assumptions') in stating that we choose the layer structure with the fewest layers to represent the sample. See Garrett (1991) for an interesting application of Occam's Razor to Bayesian probability. Thus, we make the layer structure as coarse as possible consistent with the data (the calculation method is described in Barradas *et al* (1999b)).

Note that the quality of fit obtained is outstandingly good even with these very discontinuous solutions. From an analytical point of view it serves to emphasise that we find an optimal solution; the solution is consistent with the data, leaving open the question of what other different structures may also be consistent with the data, and how different they might be. We return to these questions later, but we note here that it is clear that some sort of continuity condition ought to be applied to this type of data and we have not yet satisfactorily determined how such a condition could be specified.

5.7. RBS by the unskilled

Finally, returning to figure 1, this spectrum was from one of a set of twelve samples created in an experimental set-up as an exercise for a group of school-leavers (18-year-olds) as part of a national scheme to give this age group a taste for university research. These young people had approximately four hours training in RBS data collection and data reduction techniques. The data were collected for them and the analysis was set-up, and then they, essentially unaided, used the DataFurnace software to extract depth profiles from the whole data set, writing up the results (including a full presentation of the methods, aims and complementary optical results) in a single day. This expresses exactly the benefits of using this new software tool for solving RBS spectra. The data turned out to be very interesting and were subsequently published (Belson *et al* 1999).

6. The forward model

In this section, we explicitly state the forward model that we use, and also describe the code structure of the IBA DataFurnace, and an extension to moderately rough surfaces. We also briefly review other simulation and fitting codes.

6.1. Simulation

All IBA labs have simulation codes to calculate spectra to compare with collected data: these are equivalent to what we have called the forward model and have long been available (Brice 1973). There are a number of codes, with various useful user interface features, which have been well reviewed by Kótai (1994). The DataFurnace is not a simulation code; it is a fitting code, incorporating a simulation code in its core. It replaces all existing single scattering simulation codes (we discuss multiple scattering codes below in section 7). Because the forward model is executed repeatedly for each fit it is optimized for speed. However, some improvement of the algorithm may be obtainable using Serruys' retrograde method (1991).

6.2. Fitting

Kótai does not mention Serruys *et al*'s interesting 'PERM' code (1993) which is a true fitting code based on a novel simulation algorithm (Serruys 1991) and a novel and efficient spectrum smoothing algorithm (Serruys 1990). However, Serruys' code is not a true algorithm, relying as it does both on a reasonable initial guess by the user and also on some guidance by the user during execution.

Børgesen *et al*'s matrix inversion code ('SQUEAKIE', 1982) is a mathematical attempt to solve the inverse problem which we have already described (section 5) and which has severe limitations. A similar but much more general approach has been taken by Kogan *et al* (1994) based on the reduction method for ill-posed problems developed by Pyt'ev (1983). Pyt'ev's method is for linear cases but Kogan *et al* have generalized their treatment for this non-linear problem. Kogan's 'Beam Expert' does appear to be truly general purpose, that is, it is capable of inverting spectra where the partial spectra overlap or where there is no unique solution. However, it is also not clear how robust it is to problems of the forward model, in particular those due to errors in the energy loss database. Nor is it clear whether or not it is robust in use, or whether it has instabilities similar to those exhibited by Serruys' code.

Difficulties and shortcomings of this type of inversion code have been comprehensively and elegantly described by Cumpson (1995) for the (related) technique of angle-resolved XPS. Cumpson also compares the properties of inversion and maximum entropy algorithms (we describe the MaxEnt code of the Garching group below, section 9), and he comments on the usefulness of the MaxEnt approach, especially when uncertainty estimates are required. Our approach is mathematically closely related to the MaxEnt one.

6.3. The RBS forward model

The RBS forward model is straightforward to calculate numerically. The sample is divided into thin layers and the scattering of the incident beam (of energy E_0) from each layer is considered. Then the energy of the beam E_q before scattering after crossing layer q is given by an integration of the energy losses on the inward path to the layer:

$$E_q = E_0 - \sec\theta_1 \sum_{i=0}^{q-1} t_i \varepsilon(\boldsymbol{p}_i, E_i) \tag{3}$$

where θ_1 is the incident beam angle from normal, t_i is the thickness of the ith layer (in thin film units, that is, in $\mu\mathrm{g\,cm^{-2}}$ or equivalent units), and E_0 is the incident beam energy. $\varepsilon(\boldsymbol{p}_i, E_i)$ is the energy loss (per unit depth, in thin film units) in the ith layer which has a composition given by $\boldsymbol{p}_i = \{p_{1,i}, \ldots, p_{e,i}\}$ where $\sum_{j=1}^{\mathrm{e}} p_{j,i} = 1$ and there are e elements. The number of scattering centres $C_{e,i}$ of element e in layer i is then given by $\boldsymbol{C}_i = t_i \boldsymbol{p}_i$. Note that this structure $\{t_i, p_{ij}\}$ has the same chemical elements but a different (larger) number of layers from the depth profile $\boldsymbol{x} = \{l_i, \mathrm{e}_{ij}\}$ defined previously. The layer thicknesses t must be chosen small enough that $\varepsilon(E_{i-1}) \cong \varepsilon(E_i)$ otherwise the numerical integration will cumulate errors.

The energy loss ε is calculated from a database of the energy loss of ions in matter (Ziegler *et al* 1985) that extends across the entire periodic table for both beam and target, and for all beam velocities above about that of 50 keV H. The energy loss in any target can be calculated by linear superposition of elemental energy losses. Thus

$$\varepsilon(\boldsymbol{p}_i, E_i) = \sum_{j=1}^{\mathrm{e}} p_{ij} \varepsilon(j, E_i) \tag{4}$$

where $\varepsilon(j, E)$ is the energy loss of the beam energy E in element j. This is known as 'Bragg's rule' (Bragg and Kleeman 1905) and is usually accurate, except near the stopping power maximum for compounds of light elements such as organics, oxides and nitrides, for which deviations as large as 20% have been observed (Rauhala 1995). The accuracy of the database is limited: errors of 10% can be demonstrated even for 'well known' elemental materials like silicon (Niemann *et al* 1996, Lennard *et al* 1999).

The scattered beam has an energy D at the detector which depends on the scattering nucleus and the pathlength from the layer back to the surface, and which is calculated with an integral analogous to that of equation (3), but which we will write iteratively for clarity

$$\boldsymbol{A}_{i-1} = \boldsymbol{A}_i - \frac{t_i \varepsilon(\boldsymbol{A}_i)}{\cos\theta_2} \tag{5}$$

$$\boldsymbol{A}_q \equiv \boldsymbol{K}E_q, \qquad \boldsymbol{D}_q \equiv \boldsymbol{A}_0$$

where the calculation layers i are as before, $\boldsymbol{D}_q = \{D_{1,q}, \ldots, D_{e,q}\}$ is the list of energies at the detector from the qth layer for the e elements in the sample, $\boldsymbol{K} = \{K_1, \ldots, K_e\}$ is the corresponding list of kinematical factors and θ_2 is the exit beam angle from normal. Note that the kinematical factor is the fraction of energy that the incident particle keeps after an elastic collision (so that $\boldsymbol{D}_0 = \boldsymbol{K}E_0$), and that this fraction is calculated from conservation of energy and momentum. $\boldsymbol{A}_1 = \boldsymbol{K}E_q$ is the energy at the qth layer after backscattering and the $\boldsymbol{A}_i$ are the energies on the outward path at the ith layer.

The pulse height spectrum is obtained by digitizing each pulse from the detector with a multi-channel analyser (MCA). This spectrum is then transformed to an energy scale by a linear relation, without loss of generality since non-linear electronics can be linearized (see Lennard *et al* (1990)):

$$S_c = \gamma c + o \tag{6}$$

where S_c is the energy represented by the MCA channel number c of the spectrum, γ is the electronic gain (in keV/channel) and o is the electronic offset (in keV) due to the detector pulse height defect. The determination of γ is critical in the system calibration. Actually, γ is a weak function of c, but this dependence is usually unobservable for surface barrier detectors (see Lennard *et al* (1990), Jeynes *et al* (1998)).

We now have to transform the layer number of the sample used for the energy loss calculation into the channel number in the spectrum. Note that this transformation is neither linear with depth nor the same for different elements (see equations (1) and (2)). We calculate the layer number m corresponding to channel number c for e elements of the sample through the inequality

$$D_{e,m+1} < S_c \leqslant D_{e,m} \tag{7}$$

so that each channel corresponds to a layer at different depth for every element (e values of m for every channel c). Then the beam energy $B_{e,c}$ before scattering from element e in the layer corresponding to channel c is given by

$$B_{e,c} = E_m + r_{e,c}(E_m - E_{m+1})$$

$$r_{e,c} \equiv \frac{D_{e,m} - S_c}{D_{e,m} - D_{e,m+1}} \tag{8}$$

Of course, for each element e there is a maximum channel number k (non-integral in general) such that $S_k = K_e E_0$ (where K is the kinematical factor mentioned above). There is also a set of absolute minimum layer numbers z given by $\boldsymbol{D}_z = 0$, although the cutoff energy below which there is no useful information is usually much larger than zero.

The number of scattering centres of element e in the layer m is given by

$$N_{e,c} = C'_{e,c} - C'_{e,c+1}$$

$$C'_{e,c} \equiv r_{e,c} C_m + \sum_{i=1}^{m-1} C_i \tag{9}$$

Note that $\boldsymbol{B}_e = \{B_{e,1}, \ldots, B_{e,c}, \ldots, B_{e,v}\}$ is a list of the beam energies before scattering where the sample is divided into v layers with each layer corresponding to one channel of the spectrum, whereas $\boldsymbol{E}$ is a list of the beam energies before scattering where the sample is divided arbitrarily into equal thickness calculation layers.

A partial spectrum for element e of the sample can then be calculated through:

$$\boldsymbol{f}_e = \frac{Q\Omega\gamma \boldsymbol{N}_e \sigma'(\boldsymbol{B}_e)}{\varepsilon(\boldsymbol{p}, \boldsymbol{B})} \tag{10}$$

where σ' is the differential Rutherford scattering cross-section and the vector notation $\boldsymbol{f}_e = \{f_{e,1}, \ldots, f_{e,c}, \ldots, f_{e,v}\}$, $\boldsymbol{N}_e = \{N_{e,1}, \ldots, N_{e,c}, \ldots, N_{e,v}\}$, $\varepsilon(\boldsymbol{p}, \boldsymbol{B}) = \{\varepsilon(\boldsymbol{p}_1, E_1), \ldots, \varepsilon(\boldsymbol{p}_c, E_c), \ldots, \varepsilon(\boldsymbol{p}_v, E_v)\}$ is used as before, with v relevant channels in the spectrum for element e.

The product of the collected charge and detector solid-angle $Q\Omega$ is another critical calibration parameter.

The complete spectrum is then given by the summation of all the constituent elemental spectra:

$$\boldsymbol{F} = \sum_e \boldsymbol{f}_e \tag{11}$$

and the detector resolution is convoluted into $\boldsymbol{F}$ if required. Energy straggling (or, more generally, the depth dependent energy resolution) is convoluted into $\boldsymbol{f}_e$ if required, but this significantly increases the computation time, and therefore is only used where necessary.

6.4. Forward model changes for other IBA techniques

For EBS we simply substitute a different (numerical rather than analytical) scattering cross-section function for σ. In most cases, this is a trivial extension. However, there are many very sharp and closely spaced resonances for some nuclei (e.g. ^{27}Al) and care must be taken not to introduce integration errors in these cases (Gurbich *et al* 2002).

The ERD forward model is almost exactly the same except that the recoil rather than the scattered particle is followed on the outward path. Also we permit a range foil before the detector (for either RBS or ERD: it only requires extra energy loss on the outward path). Time of flight ERD (ToF-ERD) does not require any modification of the algorithm: it requires only being able to handle multiple spectra: for this technique

the three-dimensional data set can be separated into a series of spectra, generally one for each element. Heavy ion ERD (HI-ERD) requires no modifications: the interaction cross-sections are generally Rutherford and the stopping cross-sections are tabulated in the semi-empirical database. HI-ERD is usually carried out at a recoil angle sufficiently large for the high intensity forward scattered primary beam to be kinematically prohibited. Where this condition is not satisfied some other means must be found to exclude this beam: ToF techniques can work for a low intensity or a pulsed primary beam, or a range foil can be used with a surface barrier detector. In the latter case the different recoil ions may be superimposed in the same spectrum and cannot be separated by the detector. In any case, the DataFurnace can handle the data.

For NRA the situation is somewhat different. The model outlined above for RBS assumes implicitly that there is a monotonic relationship between depth and channel number for any particular elemental signal. This is not always true for NRA, and DataFurnace (Barradas and Smith 1999) use a different (more cumbersome) algorithm that takes this into account, unlike other NRA codes Lennard *et al* (1993) also gives a correct treatment. Otherwise, for NRA we only have to modify the kinematics formulae to allow for the non-zero Q values, introduce the appropriate interaction cross-section values (as for EBS), and specify and follow the appropriate detected particle (as for ERD).

6.5. PIXE

DataFurnace does not yet support PIXE. The PIXE forward model is entirely different in structure from the particle scattering models, and it is not trivial to modularize existing codes, such as GeoPIXE (Ryan *et al* 2002) or GUPIX (see Blaauw *et al* (2002)) for use in SA. There is not much depth sensitivity in PIXE data, just as there is often considerable ambiguity about mass in RBS, so these two techniques are highly complementary. Grime (1995) has provided a powerful user interface to give GUPIX users effective simultaneous access to RBS.

6.6. DataFurnace code structure

SA is a modular algorithm involving four modules: the forward model, the generation function, the acceptance criterion and the cooling schedule. Different functions can be substituted for any of these four modules without changing the fundamental operation of SA. Therefore, we can use different forward models with essentially no change in the code.

The DataFurnace is a hybrid code, with a preparation algorithm that characterizes the spectra and determines parameters for the SA cooling schedule, the SA algorithm itself, and a final local minimization routine that takes over at low temperatures. This latter is because although SA is a very efficient global minimization algorithm it is very inefficient at determining true local minima.

The preparation algorithm uses an adaptive filter to smooth the spectrum very effectively without significantly changing the position or width of peaks and edges, and then it counts the number of peaks and edges, used to determine SA parameters. The local minimization routine is a grid search routine which is very stable (although rather slow) in the high dimensional spaces common in DataFurnace analyses.

6.7. Roughness

The forward model described so far assumes a perfectly smooth sample surface. However, samples are rarely so smooth—perhaps the main exception being electronic samples, which is one reason why IBA has been used extensively on such materials—and surface topography introduces marked spectral distortions which cannot be evaluated without a model, introducing many more parameters in the description of the sample. These effects have been long known: a notable example is Edge's (1983) elegant use of them to characterize optical fibres and optical gratings.

Roughness problems are attracting increasing attention now that computers are so much faster, for example: Marin *et al* (1996) have extracted information about the distribution of the droplet sizes of lead on glass and copper in kapton and Niwa *et al* (1998) have done similarly for an island growth problem; Simon *et al* (1998) have analysed patterned and porous samples with the microbeam; and Slotte *et al* (2000) have shown how spectra from rough samples can be solved using IBA, AFM and SEM methods in a complementary way. In a somewhat different case, Stoquert and Szorenyi (2002) have recently published an elegant and general approach to the analysis of RBS, ERD and NRA spectra from films containing distributions of sub-micron inclusions, either spherical or columnar.

Systematic approaches have been made to the accurate calculation of spectra from general rough surfaces for RBS by Shorin and Sosnin (1992) using a Monte Carlo code and for ERD by Yesil *et al* (1998) with the SURF code.

Clearly, these sorts of codes are too slow to incorporate into DataFurnace and Barradas (2001) has implemented a simple and generally useful parametrization scheme for rough surfaces which is valid for moderate roughness, that is, provided the beam does not enter and leave the sample more than once. This approach is appropriate for thin films and multilayers with roughness values up to a few tens or hundreds of nanometer. By calculating the broadening due to roughness, and assigning it as an extra contribution to the energy straggling, an apparent energy resolution is obtained. This is then convoluted with the theoretical spectrum in the normal way. The effect of roughness can thus be included in NDF with little effort, paying only a small price in terms of calculation time.

The broadening depends on the exact type of roughness. Three different models were implemented into DataFurnace: inhomogeneous layer thickness, corrugated sample and rough substrate surface (refer to figure 4 of Barradas *et al* (1994), for a visualization of the models: this example has been reanalysed with the modified NDF code in Barradas (2002)). Interfacial mixing in multilayers can also be analysed with the method developed—see Barradas *et al* (2001) for an example in the SiGe system and Tavares *et al* (2002) for one in the TiAlN/Mo system. DataFurnace can perform automatic fits to several spectra collected from the same sample, ensuring all the information in the data is used self-consistently to obtain the final depth profile and roughness parameters. The code is also valid for ERD.

7. Forward model limitations: multiple scattering

The SA algorithm is only as good as the forward model since errors in the forward model must result in a failure to calculate the spectrum correctly from the true sample structure

(depth profile). Conversely, the DataFurnace is able to yield essentially perfect fits to the data, and forward model errors must distort the results. For accurate analysis, we have to be able to make allowances for forward model errors, and in the first example, we show how to correct for errors due to multiple scattering and similar effects. We should comment that the best DataFurnace can do is to give excellent fits to the data: there are no shortcuts to evaluating the robustness and absolute accuracy of the results, which remain the responsibility of the analyst.

7.1. RBS of O implants into SiC

Waveguides in SiC with the lowest reported losses to date have been made by high dose ion implantation recently (Vonsovici *et al* 1999). A buried oxide layer was formed by ion beam synthesis using high dose high energy oxygen ion implants. Figure 4(*a*) shows an example of the RBS spectrum from one such sample. For the sample illustrated, a continuous buried SiO_2 layer has not formed: this occurs at higher implantation temperature.

This is very clearly a good example of a 'hard' RBS spectrum since the C and O signals overlap and the profile shape is arbitrary—we know for example that the O profile is not the implanted 'Gaussian' shape that can be calculated. In this study, there were dozens of these spectra to analyse, since there was a large matrix of implantation and annealing temperatures to explore (Jackson 1998). These spectra are readily solved by SA, dramatically reducing the time and other resources needed to complete this project.

7.2. Low energy effects

The interesting thing here is that the signal comes from deep in the sample with the information being carried by very low energy backscattered particles. In these conditions our RBS forward model is inaccurate, assuming only single collisions, where actually there is a significant low energy signal coming from multiple and plural scattering. (Multiple scattering involves many small angle scattering events and plural scattering involves multiple large angle events.) These effects are well understood: Rutherford had already made reasonable estimates of multiple scattering in 1911, and accurate Monte Carlo calculations can now be made (Bauer *et al* 1992, 1993).

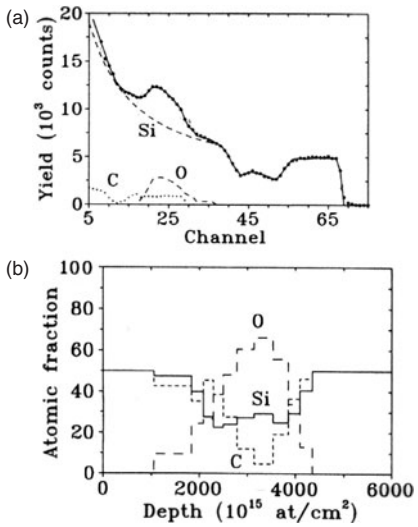

Figure 4. (*a*) RBS spectrum (· · · · · ·) of SiC implanted with 200 keV 14×10^{17} O cm^{-2} at 180°C together with the SA fit to the data (——). The partial Si, O and C spectra are also shown. (*b*) Depth profile determined by SA. Figure 2 of Barradas *et al* (1998c).

However, the forward model is core code in SA, executed for each trial $\boldsymbol{x}$ from the state space, and therefore implementing a correction in MC code is out of the question, due to the computational time involved. Mayer (1997) has given a partial solution to this problem with his SIMNRA code which implements a 'dual scattering' calculation which is able to account for much of the low energy background observed. Eckstein and Mayer (1999) give an illuminating discussion of how good the SIMNRA approximation is (it is surprisingly good!). The spectral broadening introduced by multiple scattering is calculated correctly in Szilágyi's DEPTH code (see below in 'high depth resolution' section 10).

7.3. DataFurnace correction

We here describe our *ad hoc* solution to this problem (Barradas *et al* 1998c), and discuss its effects. These multiple scattering effects cause the yield to increase at low energy. Since the increase is expected to be quadratic in the forward model (since the RBS cross-section goes inversely as the square of the beam energy) we take a faster dependence than this to be cubic as a first order approximation. We therefore compare a spectrum from unimplanted SiC with a simulated spectrum (the spectrum calculated with the forward model), and determine the cubic function that transforms one to the other. We then incorporate this function into the forward model for the Si signal, since it is a correction which applies deep in the sample, and the Si signal comes from the deepest regions. It turns out that this correction is analytically very satisfactory since it applies equally well to the spectra from the implanted samples.

Although we expect multiple scattering to modify the forward model, it should be emphasised that our correction is entirely *ad hoc*. We have simply introduced several extra fitting parameters to get a better match with the low energy part of the spectrum. Therefore, we will refer to the 'MS correction', and point out that it is a background subtraction device rather than an analytical calculation justifiable from physics.

7.4. Good fitting

Is such an *ad hoc* device of any real value? The answer is yes, for interesting reasons. SA depends on the objective function being sensitive to moves in state space away from the optimal solution $\boldsymbol{x}_0$. As mentioned in Barradas *et al* (1997), we normalize the objective function $\Delta(\boldsymbol{x})$ such that $\Delta(\boldsymbol{x}_0) \approx 1$. So if an error in the forward model means that $\Delta(\boldsymbol{x}_0) > 1$ we increase the size of the set of near-optimal solutions for any given value of $\Delta > 1$. In other words, to get a precise solution (one that discriminates reliably between similar structures) it is necessary to have a good fit.

Therefore, for a reliable interpretation of the difference between similar complex spectra like that in figure 4 we must introduce the MS correction. The question then is, how accurate is the result? We explore this question in detail later,

but in this case we note that the correction is applied to the deep part of the Si signal, is small at the depth of interest, and is analytically robust (it can be transferred from the unimplanted sample to the other implanted samples).

There are a variety of artefacts that can give rise to extra (or reduced) low energy signal, including incorrect beam handling, error in the nominal backscattering angle and electronic faults. With the use of the *ad hoc* MS correction these may affect the accuracy but not the precision of the SA calculation.

8. Ambiguity in IBA data

We will show that IBA spectra are grossly ambiguous in general, and we will re-analyse the ambiguous spectrum previously discussed masterfully by Butler (1990). There are two approaches to overcoming this ambiguity: the first is to collect multiple spectra under different conditions to constrain the solutions found, and the second is to rule out *a priori* certain types of solution which we will call 'restricting the state space'. The DataFurnace code encourages both approaches.

8.1. Multiple spectra

Every analyst has tilted the sample and taken another spectrum to determine which features of the spectrum come from the surface: the surface signal position does not vary with beam angle, although signals from below the surface will appear to move as the geometry changes. An equivalent way of doing this is to use two detectors at different scattering angles. Of course, this is not a new idea: Williams and Möller were using two (or more) detectors in 1978 (although with a rather different purpose) and Edge (1988) showed calculations emphasising the value of spectra from two detectors, but using an iterative method of calculation not easy to extend to three or more spectra. We rejected this procedure when we were considering incorporating the matrix inversion code (Børgesen *et al* 1982) into a general algorithm. Butler (1990) emphasises the value of multiple detectors and Alkemade *et al* (1990) demonstrate that for a sample with n elements, one needs to collect $n - 1$ different spectra to eliminate ambiguity in principle. However, with manual methods the analyst has to laboriously fit each spectrum in turn: this is a very large disincentive to collecting multiple data, or, even if they are collected, to analyse them (although many simulation codes give assistance with this).

SA uses a different approach: instead of asking for a spectral inversion procedure that finds the unique solution (assuming that there is sufficient information), it uses a procedure that finds any solution consistent with the data. Therefore, even if the data are ambiguous a solution can be found and the algorithm will not crash. We should emphasise that no machine methods for self-consistently inverting multiple spectra have been presented, apart from SA.

Because SA is minimizing an objective function, and since we can use a different objective function for each beam geometry, it is simple for SA to calculate a composite objective function for multiple spectra. This composite function is described in Barradas *et al* (1999d): briefly, we give each spectrum in the set equal weight irrespective of the integrated counts in the spectrum. We emphasise that SA will do its best to find a solution consistent with all the data. The computation time is affected for multiple data sets since as many simulations have to be calculated from different forward models as there are different spectra. However, the calculation is highly modularized and optimized for speed, and having calculated one forward model the others are much less tedious. Also the cooling schedule is faster for multiple spectra since we expect the minima in state space to be better defined. For both of these reasons computation time increases less than linearly with the number of spectra.

Although implementing SA of multiple data sets is nearly trivial, the resulting power made available to the analyst is enormous. Multiple detectors, or geometries, or beams, or even techniques can be used, with no penalty to the analyst in data analysis time after the calibrations have been established. We will give examples of all of these. In particular, a self-consistent analysis is very valuable in accurate work where demonstrably independent confirmation is a prime requirement to validate the measurement. Instead of repeating the analysis we only have to collect double detector data and show self-consistency.

8.2. Example—RBS of B in Si

As an example of this we have considered a nominally BCN film deposited on Si by magnetron sputtering (Barradas *et al* 1999c). These films are of interest because of a predicted hardness, stiffness and conductivity comparable to diamond. The determination of composition is actually quite difficult: it is hard (or impossible) to resolve the light elements by EPMA, even if a windowless x-ray detector is available, and e-beam induced x-ray measurements are troublesome to interpret for these very thin films. RBS, on the other hand, is not very sensitive to low Z elements, especially on a high Z substrate. However, we have shown that a self-consistent analysis of multiple spectra can be used to confidently extract and quantify very small signals. For this sample two beam energies were used, with random and channelled spectra being collected for each. The channelled spectra gave much better signal-to-noise ratios for the light elements: the MS correction was used for all spectra to fit the (channelled) Si background signals. In this case, the film composition was $\{\mathrm{B, C, N, O, F}\} = \{15.6(2.1), 7.0(3.1), 30.9(0.9), 37.7(0.6), 8.8(0.4)\}$ where the (1 sigma) statistical error is given in brackets. The detection limit for B in this analysis was 7 at% (99% confidence).

8.3. Example—spectra with large dynamic range

This is a rather different example. Often samples are analysed which have (relatively) heavy element minor constituents with a light element matrix. Thus, Mallégol *et al* (2002) have analysed surface treatments of latex films where the interest is in the distribution near the surface of elements characteristic of surfactants. These spectra have to be displayed on a log scale, and a simple use of DataFurnace results in the minor elements being simply ignored since the number of counts are not sufficient to affect the χ^2 sum by much. In this case, we can split the spectrum into two (or more) parts, and combine the χ^2 for the separate parts in the same way that we did for separate spectra. Then a good fit is obtained for the whole spectrum. The only problem to mention is that DataFurnace must not

be allowed to change calibration constants (including charge) independently for these split spectra.

8.4. Restricting the state space

It is very easy to demonstrate that RBS spectra are ambiguous: the mixed silicide sample of figure 2 could have metal deep in the sample for example, as discussed in Barradas *et al* (1999b) (BJJM99). Butler (1990) has shown an example which is ambiguous in the sense that different depth profiles exist where different partial spectra add up to the same total spectrum: we discuss this interesting case below. However, we have not (yet) found any examples where IBA data are systematically ambiguous in the sense that the system is 'frustrated' in Kirkpatrick *et al*'s (1983) terminology; that is, where different optimal solutions exist between which are large potential barriers.

When interpreting such data as the mixed silicides described above (figure 2) analysts are used to ruling out the possibility of metal deep in the sample because they know that in this case the substrate is pure silicon. However, we have demonstrated that the most probable solution of this spectrum, assuming that there is no prior information, is that there is some 5 at% metal in the substrate (BJJM99). It is important to be objective about what we know about the sample *a priori*. If we assume nothing about the sample then we have to give a range of possible solutions, consistent with the data. We did this crudely using the MCMC code to simply specify an 'error bar' on the calculated depth profile (see below section 9). The median solution has substantial metal and over 50 at% O for the substrate. The MCMC code determines the most probable solution, and explores state space around it, effectively determining the density of states in state space. Because we only calculate the variance of this distribution of states we will clearly not recognize bimodal, skew or any other non-normal distributions. Of course, much more sophisticated statistics are available from an MCMC treatment.

Interestingly, we also used this mixed silicide example to demonstrate that provided the state space is suitably restricted the RBS data are remarkably unambiguous with respect to collected charge (total number of counts). It is common for analysts to collect large amounts of charge to get 'smooth' data, but very small charges (we show 0.1 μC with 2.5 msr detector solid-angle, BJJM99) can give objectively quite well-determined solutions even for this 'hard' case, with the right number of layers and qualitatively the right stoichiometry in the layers. Of course, with less counts in the spectrum the statistical errors on the stoichiometry and layer thickness increase as expected.

This example makes it very clear that the spectra are grossly ambiguous in principle, and we have to give the analyst tools for excluding regions of the state space which have a high density of false solutions. The solution we want, with a pure silicon substrate, is a perfectly good solution. However, it is unique; a singular solution, and to find it we have to explicitly exclude the 'infinite' number of solutions involving an impure substrate. This is easily done in practice by specifying the depth and concentration range for one or more of the elements, and constructing the generation function appropriately. It is possible to overspecify the state space restrictions so that the code cannot find any solution: in this case the code will give a warning, and the 'solution' found will not fit the data! Actually, for figure 2, the only restriction required is for the O to be limited to the near-surface region.

8.5. Butler's example re-analysed

Butler (1990) takes a different approach with an example of an oxidized NiCrAl alloy that we show in figure 5. He points out that for this example the false solutions can be eliminated if prior chemical information is taken into account. Thus, he knows that the oxygen comes from the oxidizing process, and therefore enters through the surface. (Actually, most of his false solutions are eliminated simply by excluding O from the substrate.) Moreover, the O binds with the metals in well-known ways. In his simulation code, he gives the analyst tools to manipulate molecular (rather than atomic) depth profiles.

We do the same thing by allowing the analyst to specify molecules rather than (or as well as) atoms. Figure 5(*a*) shows the elemental depth profile of Butler's example with a spectrum calculated from it (figure 5(*b*)). We then ask DataFurnace to invert this spectrum to retrieve the profile under a variety of assumptions. Figure 5(*c*) shows the closest DataFurnace could get to the original profile, and we discuss this result further below. We point out here that the result is essentially identical to the original, except for some interface broadening (we have not deconvoluted the straggle).

It turns out that the Cr profile is the most sensitive to the prior assumptions of the analysis, and figure 5(*d*) shows the Cr profiles obtained by DataFurnace under four different assumptions. To retreive Butler's initial profile unambiguously we need to specify not only the molecules present but also that only oxides are present near the surface and that oxygen is excluded from the substrate and that Al is excluded from the near surface region and that two independent spectra are taken (at different scattering angles in our example). Butler did not point out this last condition for this example, although he noted that, in general, multiple spectra are always a help. These particular data are very ambiguous: excellent fits can be obtained without any of the conditions mentioned, and they are all as good as that shown in figure 5(*a*).

In this example, we have only allowed the O to exist bound to metals, and we have only allowed free Ni to exist. The substrate is specified by a molecule representing the starting alloy composition. Of course, DataFurnace does not require the analyst to input anything else: the fit proceeds automatically as soon as the initial assumptions are stated. The interesting thing is that it is very easy to specify various assumptions about the chemistry to see whether they are consistent with the data. If they are not consistent they can be ruled out. Now the analyst has an effective tool not just for obtaining a solution to a spectrum, but for testing a variety of assumptions about the sample against the data.

We must emphasise that we can only extract information from a spectrum if the information is really there. DataFurnace cannot extract more information than exists! But DataFurnace can be used as a tool to explore the validity of various prior assumptions about the sample. It can also be used as a tool to explore what further information would be useful to reduce ambiguity.

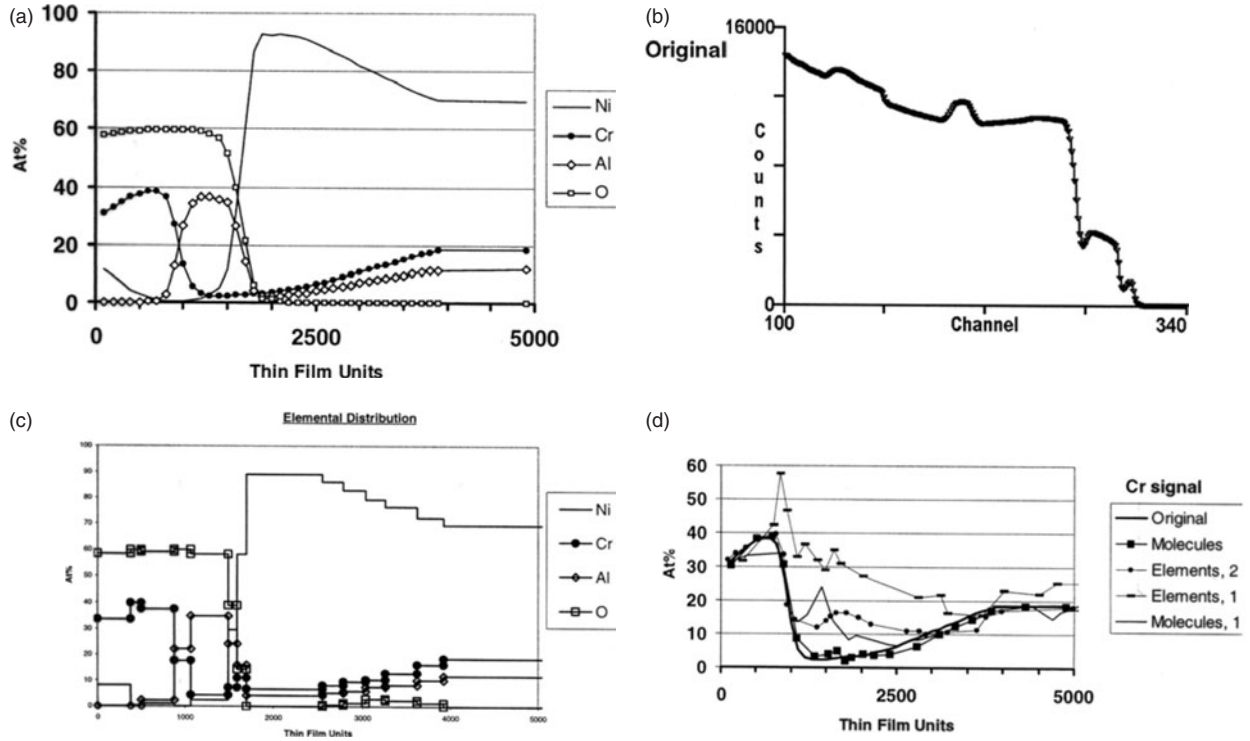

Figure 5. Re-analysis by DataFurnace of the data shown by Butler (1990) of an oxidized NiCrAl alloy. (*a*) The original profile from which the spectrum was calculated; (*b*) spectrum (symbols) and fit (line); (*c*) atomic profile fitted to data assuming molecules and complete oxidation from the surface, using two spectra at different detector angles, and excluding alumina from the surface; (*d*) a comparison with the original profile of the Cr profile calculated under various assumptions. Specifying only elements barely constrains the profile, and even with two detectors the profile is not recovered at intermediate depths. Using only one detector with the assumption of molecules is also not sufficient. Molecules used are NiO, Cr_2O_3, Al_2O_3 and Ni_{195} Cr_{186} Al_{119}.

8.6. Polymer example

Ross *et al* (2001) have used RBS in conjunction with XPS and other surface specific techniques to investigate the alkaline treatment of poly(vinylidene fluoride) samples in the presence of phase transfer catalysts. This is a very difficult analysis since the spectra are relatively featureless and are thoroughly ambiguous in the absence of any chemical information in much the same way as Butler's mixed metal oxide example above. However, the analysis is successful when the chemical state of the various elements is specified. The defluorination kinetics was shown to follow the Fickian diffusion law with a treatment depth of over a micron. Interestingly, to complete this work a large batch of several dozen samples had to be analysed.

8.7. Examples of ERD

DataFurnace can accept a wide variety of analytical conditions. ERD is interesting since it is used in widely different ways in different labs. Barradas *et al* (1999d) analysed a silicon oxyfluoride film using 35 MeV Cl^{5+} with two separate beam geometries and three different detectors including a silicon surface barrier detector with a range foil specifically for recoiled H, a Bragg detector and a time of flight (ToF) detector. The latter two detectors have similar signals but different surface sensitivities. It is interesting that DataFurnace can easily cope with the signal overlaps that are so inconvenient for manual analysis in all of these detectors in the same way that it does for RBS spectra. Of course, the practical difficulty with this sort of analysis is that one is often overwhelmed with information. In this example, there are ten different spectra available, each carrying different information. All ten were fitted simultaneously with the DataFurnace, which also weights them according to their sensitivities in a completely objective way. This is also a good example of multiple analyses being done with a variety of techniques, detectors in this case. The data is very easy to collect, and now, with the DataFurnace, it has become very easy to analyse.

It is also possible to do very satisfactory H determination using ERD with a 1.5 MeV $^4He^+$ beam and a 6 μm mylar foil to range out the forward scattered ^{4}He primary beam. A good example is shown in figure 6 (Barradas *et al* 1999a), where we were trying to synthesize an amorphous GaN by implanting an amorphous hydrogenated silicon nitride with Ga. Crystalline GaN is an exciting material for blue LEDs, for example, but it is believed that the amorphous material could also be very interesting, perhaps for applications like large area displays.

However, it is hard to make GaN, and ion beam synthesis was an interesting possibility. The question following the implantation is, does the Ga substitute for the Si or the N? The RBS on its own is equivocal in the presence of so much hydrogen, but with the clear H signal obtained with the ERD (showing H loss near the surface due to the implant) an accurate profile calculation can be made using the right function of energy loss with depth. This data suggests that in this case the Ga is substituting for Si, implying the presence of GaN. We

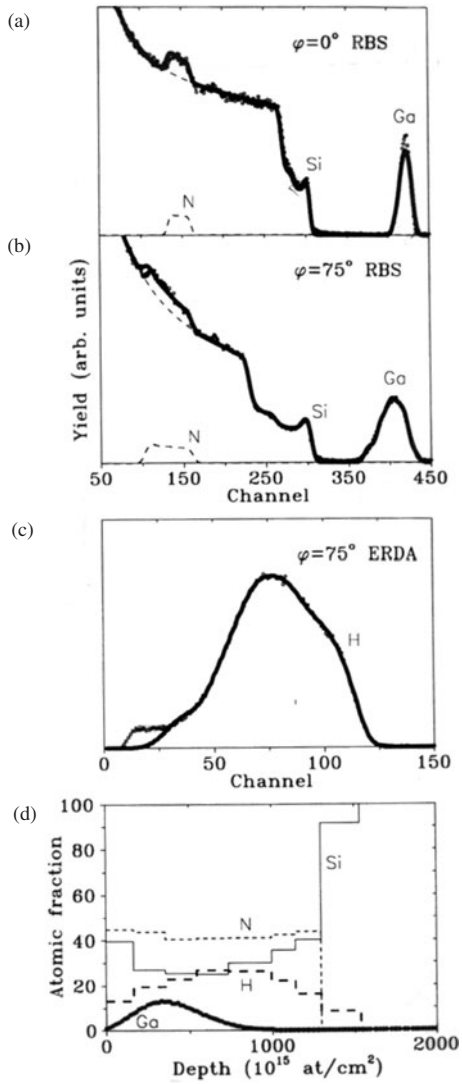

Figure 6. RBS/ERD of PECVD a-SiN_x : H implanted with 75 keV 75×10^{15} Ga cm^{-2} and annealed in N_2 for 30 min at 200°C. (*a*) RBS, normal incidence. (*b*) and (*c*) RBS and ERD respectively, collected simultaneously with backscattering angle 150°, recoil angle 26°, beam incidence angle 75°. The solid lines are the fits; N partial spectra are shown. (*d*) Fitted depth profile. Figure 3 of Barradas *et al* (1999a). Also see figure 8.

consider the precision of this result in the next section. GaN bonding has been demonstrated by XPS (Almeida *et al* 1999). It turns out that this only occurs where the a-SiN_x has excess nitrogen.

9. Precise IBA: quantifying the error by Bayesian techniques

In the example of the ion beam synthesized GaN above (figure 6) we extracted a depth profile that showed a negative correlation between the implanted Ga and the Si concentration. As it stands, the result is only suggestive because it is not clear, and it certainly has not been demonstrated, that profiles for which this negative correlation does not exist are excluded by the data. The given profile is demonstrably consistent with the data but other qualitatively different profiles have not been shown inconsistent with the data. Clearly, one could play with the profiles and a simulation code and convince oneself that a different conclusion is excluded, but to convince a sceptical observer a more systematic approach is required. In this section, we will show that our MCMC methods can easily be applied to estimate the likelihood of a particular profile, given the data.

9.1. Previous work

Various workers have addressed this problem in different ways. Doolittle (1986) noted that the local minimization technique in his popular program 'RUMP' yielded a Hessian matrix whose covariance represents the uncertainty. However, the minimization provided by RUMP is rather unstable and in any case depends on the user to get a solution which is nearly correct. Børgesen *et al*'s (1982) matrix inversion code also yield uncertainties naturally but these are not implemented in the distributed ('SQUEAKIE') code, which in any case requires the user to separate the elemental signals, as we have noted above.

9.2. MaxEnt

Fischer and co-workers (1997, 1998) have approached the problem from a completely different angle. They have used Bayesian statistics, with a maximum entropy prior, to deconvolute the detector resolution from RBS spectra of a Co thin film, improving the real depth resolution by nearly an order of magnitude, and resolving the signals from the isotopes of Co.

Unfortunately, this astonishing feat involves not only heavy computation but also detailed knowledge of the detector transfer function (the detector resolution, which is a function of detected energy, and may not be very stable). The group (following our work) used the same methods to extract depth profiles from RBS spectra of thicker films (Prozesky *et al* 1999), and they have also demonstrated reliable background subtraction for PIXE spectra (Padayachee *et al* 1999) and even extracted some depth information from PIXE data (Prozesky *et al* 1997). Of course, the precision of a result is yielded intrinsically by this method.

Maximum likelihood techniques have been used by Liew *et al* (1994) to extract depth profiles from PIXE spectra. Rokita *et al* (1997) have also used maximum entropy to improve the spacial resolution of microbeam PIXE maps.

9.3. Simulated annealing

We can understand Fischer *et al*'s maximum entropy calculation to be analogous to a Fourier transform of state space: it is carried out in reciprocal space, to use an analogy from crystallography. This is because it is natural to work in Fourier space when a convolution function (the detector resolution function) is central to the problem. Our SA calculation, on the other hand, is carried out in real space: state space is explored with a series of real depth profiles $\boldsymbol{x}_i$. Because we do not work in reciprocal space we have at least an order of magnitude less computation. However, uncertainty information is yielded equally naturally by our SA formalism.

We wish to quantitatively evaluate the precision of the determination of any given profile. Looked at another way,

we wish to determine the size of the set of near-optimal solutions, which we can denote by $\{\boldsymbol{x}_{0+\delta}\}$, with objective function $O(\boldsymbol{x}_{0+\delta}) = O(\boldsymbol{x}_0) + \delta$ for any given value of δ. How much can we perturb the solution we have obtained, and still get an acceptable result? Of course, from a Bayesian point of view all states $\boldsymbol{x}$ are assigned a probability, with the states $\boldsymbol{x}_0$ having the highest probability. In SA, we construct a sequence of Markov chains with reducing 'temperature', but we choose the cooling schedule such that as soon as each Markov chain is long enough to be near to equilibrium we reduce the temperature and start constructing the next Markov chain. If, instead of doing this, we construct a long Markov chain and ignore the initial non-equilibrium part, what we have is a set of states selected randomly from state space according to the probability given by the density of states.

9.4. Bayes theorem

This can be treated formally with Bayesian methods (cf Barradas *et al* (1999b)). Because of the existence of measurement error (including statistical noise and uncertainty in the experimental parameters), the observed spectrum $\mathbf{Y}$ can be treated as a probability density function $p(\mathbf{Y} \mid \boldsymbol{x})$ ('the probability of $\mathbf{Y}$ given $\boldsymbol{x}$'), which can be calculated simply by using the forward model together with Poisson statistics (although we are not restricted to a Poisson distribution). Then if we can sample from $p(\boldsymbol{x} \mid \mathbf{Y})$, the probability density function for the depth profile $\boldsymbol{x}$ given the observed spectrum $\mathbf{Y}$, we can also calculate the mean solution $\langle \boldsymbol{x} \rangle$ and the standard deviation $\sigma(\boldsymbol{x})$. But Bayes' theorem (1763; for an introduction to Bayesian methods see Lee (1997)) states:

$$p(\boldsymbol{x} \mid \mathbf{Y}) = \frac{p(\mathbf{Y} \mid \boldsymbol{x})p(\boldsymbol{x})}{p(\mathbf{Y})} \tag{12}$$

where the prior distribution, $p(\boldsymbol{x})$, represents any knowledge we have of the sample before we do the analysis. $p(\mathbf{Y})$ is independent of $\boldsymbol{x}$ and is treated as a constant of proportionality. Then the general theory of Markov chains (see, e.g. Gilks and Richardson (1996)) tells us that the posterior distribution, $p(\boldsymbol{x} \mid \mathbf{Y})$, is given by the equilibrium distribution of a Markov chain constructed with a Metropolis criterion.

9.5. Error calculation

In order to calculate the confidence interval of any particular solution, and hence find all the plausible solutions, we run a Markov chain based on sampling from $p(\boldsymbol{x} \mid \mathbf{Y})$ and use this sample to calculate the simple statistics $\langle \boldsymbol{x} \rangle$ and $\sigma(\boldsymbol{x})$. In practice, it is sensible to start this chain at a solution $\boldsymbol{x}_{\mathrm{SA}}$ obtained from SA, and let it run long enough to get reliable estimates of the moments. There are very strong links between the MCMC algorithms required by the Bayesian approach and SA, the main difference being that the MCMC algorithm stores a large set of plausible solutions calculated during a run rather than simply the final state stored by SA. This is an extra overhead with a penalty in the computation time, but the advantage is that both the average solution $\langle \boldsymbol{x} \rangle$ and the most probable solution $\boldsymbol{x}_{\mathrm{mp}}$ are determined, together with a reliability estimate $\sigma(\boldsymbol{x})$. Note that in general $\boldsymbol{x}_{\mathrm{SA}} \neq \langle \boldsymbol{x} \rangle$ (and also $\boldsymbol{x}_{\mathrm{SA}} \neq \boldsymbol{x}_{\mathrm{mp}}$) and therefore the Markov chain is run for a 'burn-in' period of a few thousand proposals before calculating moments.

From the set $\{\boldsymbol{x}_{0+\delta}\}$ of possible solutions it is possible to calculate confidence intervals for the structure of the sample. The information in these confidence intervals can be insightful for the analyst as is shown by the following simple example of the mixed metal silicides discussed with figure 2 above.

Consider estimating the total amount of each element up to a given depth in the sample. Both algorithms will give estimates of such a quantity, with the MCMC algorithm being able to also calculate the standard error of these estimates. Such standard errors can tell the analyst much about the quality of the information in a spectrum.

Figure 7 shows data from an MCMC analysis of a mixed metal (Fe and Co) silicide spectrum (these data were actually derived from the spectrum shown in figure 2 of Barradas *et al* (1997); this is similar to our figure 2 above). Figure 7(*a*) shows a plot of the set of estimates of the total amount of Fe compared to the corresponding estimate of the total amount of Si. This set of solutions clusters around the SA solution (showed by the solid lines). The spread of the set shows the degree of uncertainty in the solution. For example, the SA estimate for the amount of Fe is 262×10^{15} atoms cm^{-2}, while the MCMC calculates the standard error of this as being 1.7%.

This analysis can do more than simply calculate standard errors, useful as that is. Figure 7(*b*) show the result for Fe and Co. Note the much higher negative correlation in this plot compared to the left-hand side plot. What this is showing the analyst is that the information in the spectrum about the amount of Si is reasonably independent of the information on the amount of Fe (since the contours are nearly circular in figure 7(*a*)): however, there is very strong dependence in the information about the two metals in the sample. This analysis

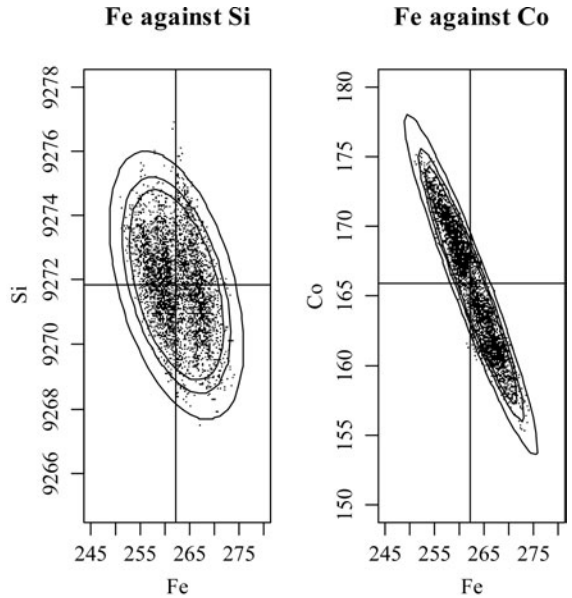

Figure 7. Plots of the Fe/Si and Fe/Co ratios from an MCMC analysis of the mixed silicide spectrum in figure 2 of Barradas *et al* (1997) (similar to figure 2 in the present work). The solid contour lines represent the 90%, 95% and 99% confidence intervals calculated by MCMC. The axes are in thin film units (10^{15} atoms cm^{-2}) and represent the total number of atoms of each species in the film.

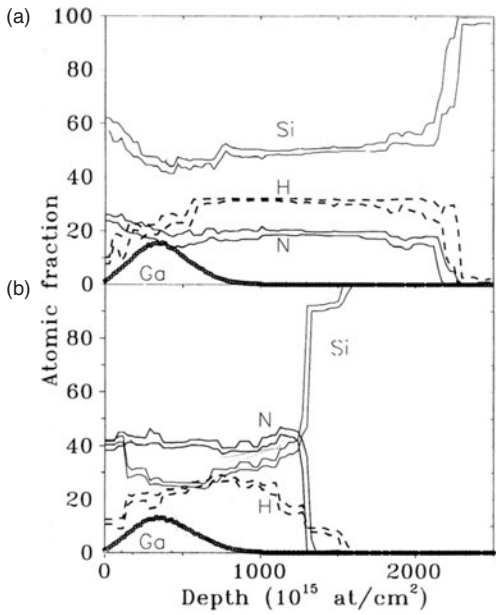

Figure 8. Confidence intervals of the Ga implanted samples of figure 6 calculated by MCMC. (*a*) Ga implanted into Si-rich SiN_x does not substitute preferentially for Si (shown in figure 6); (*b*) Ga implanted into Si-poor SiN_x (not shown in figure 6) does substitute preferentially for Si (forming GaN, as shown by XPS). Figure 2 of Barradas *et al* (1999a).

shows clearly that the spectrum gives a very precise estimate about the total amount of metal but is much less informative about the exact proportions of each. Such ambiguity could be resolved by adding molecular assumptions to the analysis. We will report elsewhere on the further development of general mathematical tools based on MCMC for investigating intrinsic spectral ambiguity (Marriott *et al* 2002).

We have applied a simple MCMC implementation to the GaN : H data of figure 6 and obtained the result shown in figure 8. For each element, the lines show ±one standard deviation from the expectation value of the depth profile. This is a direct representation of the analysis precision: the conclusion that was suggested by the SA result is confirmed by the MCMC calculation.

10. High depth resolution RBS

10.1. Energy resolution at glancing incidence

Analysts have long looked for optimum depth resolution from RBS by using glancing beam incident or exit geometries to geometrically enhance the path lengths and hence the energy loss in thin surface layers. Williams and Möller (1978) gave a detailed analysis of the individual contributions to the energy resolution as a function of depth two decades ago. We show here how the more accurate calculations carried out by the DEPTH code of Szilágyi *et al* (1995), can be incorporated into high resolution RBS (HR-RBS) measurements on SiGe multilayers. DEPTH has been validated at the 10% level for many systems including pure Si (Szilágyi and Pászti 1994), Co/Re multilayers (Barradas *et al* 1994), and Si/Ge multilayers (Barradas *et al* 1998d).

10.2. SiGe multilayers

Integrated optoelectronics on silicon using a process compatible with current silicon technology would revolutionize the industry. There is consequently intense interest in possible materials, and technologies for this. We have already mentioned β-$FeSi_2$: another possibility is the use of $SiGe_x$ alloys, which can be grown coherently on a Si substrate for a variety of heterojunction devices. Because of the mismatch of the Si and Ge lattices these layers are heavily strained and must be very thin to be defect-free. Now the growers need to know not only the thickness and stoichiometry of their layers, but also the interface quality. It would be very desirable to do this by RBS if possible, since RBS is non-destructive for this type of sample, the measurements are rather rapid, and it is valuable to have an independent technique to compare with TEM and SIMS (both destructive techniques, with TEM being very time consuming as well).

Barradas *et al* (1999f) have investigated a nominally $(Si\ 30\,nm/Si_{0.78}Ge_{0.22}\ 5\,nm)_{\times 5}$ multilayer using HR-RBS. They also used HR-SIMS and other techniques to characterize these samples. When the beam is incident normally on the sample the typical depth resolution for this system with RBS using, say, 1.5 MeV He^+, is about 40 nm near the surface. But if a glancing angle of incidence is used the resolution (near the surface) can be improved to sub-10 nm. The depth dependent energy resolution was calculated using the DEPTH code of Szilágyi *et al* (1995). We were able to obtain the probable Ge profile at sufficient precision to show that the probable mean layer thicknesses (characterizing the interface roughness) change with growth temperature. Figure 9 shows the data for a multilayer grown at 550°C, and the solutions compared for this sample and another grown at 810°C.

The solution in figure 9(*e*) showing the probable layer thicknesses indicates that there is a systematic increase in the layer thicknesses for the low temperature film. Figure 10 shows the error on the profile calculated with the MCMC method (similarly to the example of GaN : H shown in figure 8 and described above): again, the indication given by SA is confirmed by MCMC.

10.3. High depth resolution by RBS?

This very remarkable example deserves detailed discussion. The first general question is, how can useful information about the interfaces of films 5 nm thick be obtained with a system whose declared depth resolution at the film surface is 7.5 nm? The first answer to this is that while a depth profile will be broadened by the system resolution, and fine details will be smeared out, information about moments of distributions are available at much greater precision than the system resolution. For example, IBA analysts use this all the time to determine the electronics gain: we routinely acheive a precision in the determination of the position of surface signals a factor of 20 better than the nominal energy resolution of the system (cf Seah *et al* (1988), Jeynes *et al* (1998)). The second answer is that in principle the system resolution function can be deconvoluted out of the data. This can be done indirectly as we do in this example, by including the depth dependent energy resolution in the forward model. As we have already pointed out, it can also be done directly using maximum entropy (Bayesian)

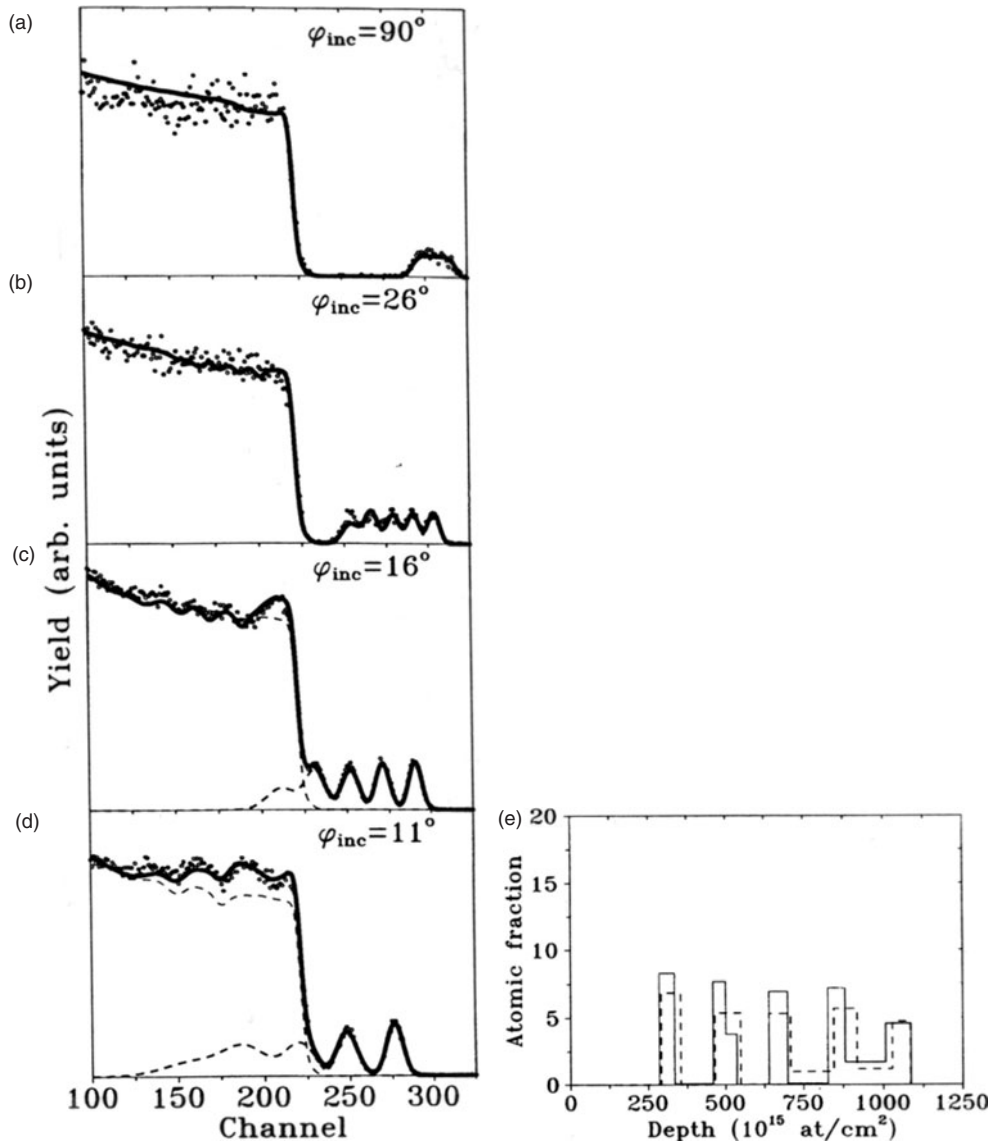

Figure 9. Above: normal incidence and HR-RBS data of a nominally (Si 30 nm/$Si_{0.78}Ge_{0.22}$ 5 nm)$_{\times 5}$ multilayer grown by MBE at 550°C. The solid lines are the fits and the dotted lines are the Si and Ge partial spectra. 1.5 MeV ^{4}He and detector in Cornell geometry with scattering angle of 160°. Below: fitted Ge depth profiles for the data shown (550°C, - - - -) and for 810°C (——). The depth resolution function is calculated with the DEPTH code (Szilágyi *et al* 1995). Figures 2 and 4 of Barradas *et al* (1999f).

techniques (Fischer *et al* 1997, 1999) with astonishingly good results but at the cost of considerable computational difficulty.

10.4. Accuracy

The second general question is, how confident can we be of the accuracy of the result? We are, after all, putting considerable weight on the interpretation of very small features of the data. There are two aspects to accuracy: the relative accuracy (that is, the precision) of two profiles, and the absolute accuracy of a profile. The relative accuracy reflects the confidence with which we can discriminate differences between samples and which we have discussed in detail in the section on Bayesian techniques and which has been calculated for figure 9 in figure 10. To estimate the absolute accuracy implies a full error analysis as described below in the sections on accuracy and on the forward model limitations.

10.5. Use of the DEPTH code

The DEPTH code of Szilágyi *et al* is central to including accurate energy resolution values into the forward model. If this is not done correctly it is not possible to fit the data properly, and the objective function starts to become meaningless since it merely reflects forward model shortcomings. DEPTH calculates the energy resolution as a function of depth due to instrumental factors such as the beam energy width and the detection system resolution, the geometrical broadening in the detector due to finite detector solid-angle, finite beam spot size and angular spread; and the energy straggling and multiple scattering which are the factors dependent on the sample. Although the simulation code RBX of Kótai (1994) effectively incorporates DEPTH internally, other simulation codes use Bohr straggling as an approximation to the energy straggling function, with a user-supplied factor to correct the values. This is quite unsatisfactory, especially as the functional

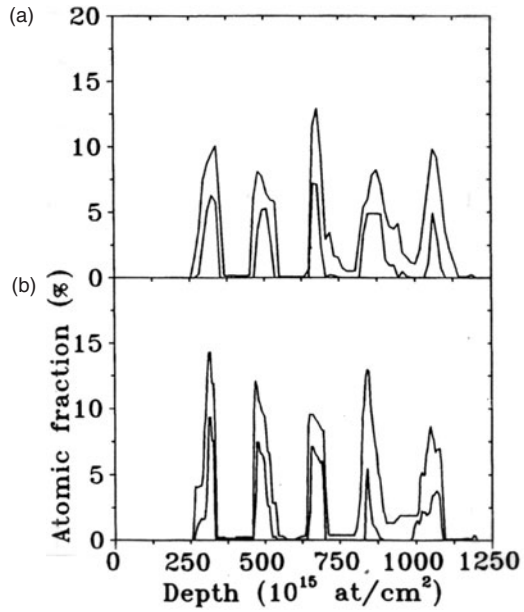

Figure 10. MCMC error calculation for the two samples of figure 9(*e*). Multilayers grown at a) 550˚C and (*b*) 810˚C. Figure 6 of Barradas *et al* (1999f).

form is not necessarily accurate. Multiple scattering is the excess energy straggling due to multiple low angle collisions. The DEPTH code does not calculate the low energy tails and other effects due to plural scattering, that is, multiple large angle collisions. Of course, plural scattering effects cannot be represented as a depth dependent energy resolution effect: plural scattering gives the specific spectral distortion of low energy tailing. This is outside the scope of this review, except to say that our MS correction will in many cases (including that of figure 4) also adequately correct for plural scattering in an *ad hoc* way.

DEPTH directly calculates the energy resolution as a function of depth, assuming a particular sample structure. Therefore, in principle, the calculation is implicit, relying on iteration to complete it. The sample depth profile must first be extracted from the spectrum without the depth resolution function, then the DEPTH calculation is done using this approximate profile, and then the SA is done again using the energy resolution function calculated by DEPTH. In fact, it was not necessary to iterate since there is very little difference between the energy resolution function calculated with and without the correct profile. However, including the depth dependent energy resolution function in the forward model considerably increases the forward model computation time, and therefore also the DataFurnace calculation time (which can be hours) since the forward model is at the core of SA.

10.6. Information from multiple spectra

In figure 9, the multilayer cannot be resolved with the beam at normal incidence (figure 9(*a*)). Even with a glancing incidence angle of 26˚ (figure 9(*b*)) the layers are only partially resolved. However, as the glancing angle is decreased the Ge starts to overlap with the Si signal and the signal to noise ratio for the deepest layers decreases. Thus, for a glancing angle of 16˚ (figure 9(*c*)) there is most information about the top three (or four) layers, whereas for 11˚ (figure 9(*d*)) there is most information about the top two layers. DataFurnace handles all these spectra together self-consistently, with the highest resolution information being available about the top two layers. Notice that the overlap of the Si and Ge signals in figure 9(*d*) causes a complex spectrum. Notice too that the spectrum is dramatically broadened for the deeper layers, and that the DEPTH calculation accounts for this correctly. This work is therefore a validation of DEPTH since unless the depth dependent energy resolution function is correctly calculated a good fit to the spectra at all angles of incidence will not be available simultaneously.

The result is shown in figure 9(*e*), which also shows a profile from a second sample grown at the higher temperature. These profiles are consistent with the data. As discussed above, the solution is given in terms of the minimum numbers of layers and compositions consistent with the data. What we fit is an estimate of mean layer thickness, equivalent to a second moment of the distribution. The energy resolution is convoluted into the spectrum calculated from the profile: the worse the energy resolution is, the less sensitive to small changes in the profile the data will be.

10.7. Error estimate by MCMC

Thus, the suggestion in figure 9(*e*) that the fourth and fifth layers merge into each other must be tempered with the knowledge that we do not have much information about these layers: many other profiles may also be consistent with the data. Again, we apply a Bayesian analysis of the expected error in these profiles and obtain figure 10. Now the likelihood that the profiles from the two samples are really different can be evaluated more quantitatively. The samples grown at the lower temperature do have rather thicker layers at lower average Ge content, consistent with the interface broadening inferred from Raman spectroscopy. What is not included in this plot is estimates of the probable number of Ge atoms in each layer together with layer thicknesses and estimates of the error on these estimates. This information is also available to the user from the Markov chain calculation.

10.8. Non-resonant NRA

Workers at Surrey (Payne *et al* 1989) were the first to use deuteration and the D(^{3}He,p)^{4}He reaction to follow the intermixing of polymers, although Lennard *et al* (1993) have thoroughly described the profiling of D using a ^{3}He beam in various Zr-based alloys. Barradas and Smith (1999) describe the analysis with DataFurnace of a multilayer of (hydrogenated) polystyrene (PS) and deuterated polystyrene (DPS) with a very high depth resolution of <6 nm. DEPTH (Szilágyi *et al* 1994, 1995) was essential for this work. The calculation of confidence intervals with MCMC confirms the multilayer structure.

Functionalized polystyrene blends have been analysed by Wendler *et al* (1999) using a very complete analysis first by simultaneous NRA/RBS with a ^{3}He beam and then by ERD/RBS. ^{4}He ERD of deuterated polymers using a detector with a range foil yields recoil spectra where the D and H

recoil signals overlap. As mentioned above, the DataFurnace code handles this case too. All glancing incidence work, including ERD and high resolution analysis, depends on a very good knowledge of the geometry of the analysis. This geometry can be determined as one of the parameters of the data analysis if multiple spectra are collected at different beam incidence angles (since relative incidence angles are known more accurately than absolute ones). This approach is powerful in determining the accuracy of the analysis (that is, yielding a result which can be certified by reference to international standards) since the data themselves imply the instrumental parameters. However, a large number of spectra are collected: in this case, we have analysed at least 13 per sample.

Barradas *et al* (2000b) show an analysis of a nitrided steel by NRA/RBS with a 1.4 MeV D beam and ERD with a 35 MeV Cl beam. Two separate analyses were made by ERD, one using a standard ToF detector and the other an angle-resolving ionization chamber. The NRA reaction was the $^{14}\mathrm{N}(d,\alpha_1)^{12}\mathrm{C}$ with $Q = 9.146$ MeV. This looks deepest into the sample but with a poorer depth resolution than the ERD. Three different N profiles were thus obtained with different depths of analysis: these are handled together self-consistently by the DataFurnace which automatically weights the data from each spectrum according to its individual sensitivity.

11. Absolute accuracy in IBA

The precision of an analysis, that is where similar samples are compared, has been considered above. However, the ultimate consideration of all analysis is the accuracy available. We use accuracy here in the critical sense, that is where a measurement can be traced back to international standards of mass, length and time with a specifiable uncertainty. Because the Rutherford cross-section is analytical the accuracy of RBS is potentially unlimited—except for the major problem in all IBA, the limited knowledge of the energy loss of ions in matter that we consider in detail in the next section. However, there are certain sorts of analysis where the energy loss enters only in second order: one of these cases has been treated in detail by Jeynes *et al* (1997) with the conclusion that even in this ideal case there are several small effects that have to be considered (at the $\frac{1}{4}$% level) that will cumulatively make an accuracy better than 1% hard to acheive. (We quote all errors here at the 1σ confidence level.)

The only query about the potential accuracy of RBS to our knowledge is the interpretation of the low energy tails in backscattering spectra. Tails are certainly caused by multiple and plural scattering effects and have been calculated successfully with Monte Carlo techniques by Bauer *et al* (1992, 1993), and most recently by Eckstein and Mayer (1999) for low energy beams where the effects are large. They could also be caused both by slit scattering and any low energy component there may be in the beam. However, a careful experiment by Gurbich (1995) used time of flight techniques with a high energy pulsed beam (2 MeV protons) and very thin foils (self-supporting gold at about 10 keV thick for this beam), with the result that he found large unexplained tails, at about 10% of the size of the expected backscattering from the thin foil.

We point out, parenthetically, that we believe that it is harder than generally supposed to establish the energy calibration with an accuracy better than 1%. Although the machine energy can be established readily at about 0.1%, the electronics calibration depends on an accurate knowledge of the pulse height defect of the detector. This has been comprehensively described recently by Lennard *et al* (1990), and we have presented a full analysis in a particular case where the best demonstrable accuracy was only 0.5% (Jeynes *et al* 1998). Lennard *et al* (1999) do not make a comparable accuracy estimate explicitly, but their work is consistent with an accuracy of about 0.5%. We are not aware of any other work that establishes the absolute electronics calibration accuracy.

Apart from issues of energy calibration, accuracy in RBS turns on knowledge of the product of the detector solid-angle and the collected charge, the so-called charge · solid-angle product, since very careful work from two decades ago established the validity of the analytical RBS cross-section when the electron screening effect was taken into account. The accuracy of the corrected RBS cross-section is usually better than the $\frac{1}{2}$% cited by Wätjen *et al* (1992) for the worst case of Bi, which is of course very heavy. Solid-angle is troublesome to measure accurately at the 1% level, as is routine charge collection in RBS systems, and analysts have used standard (certified) samples for a decade to avoid routine use of absolute values of charge and solid-angle.

The existing standard samples are Bi implants into Si, the Bi contents of which are certified at 2% (Wätjen and Bax (1994), Tesmer and Nastasi (1994)). A new set of Sb implanted samples are now available from IRMM, Geel and BAM, Berlin, and are certified at 0.6% (registered as IRMM-302/BAM-L001: Pritzkow *et al* (2001), Ecker *et al* (2002)). These samples supercede the Bi implant samples.

11.1. Implanted silicon standards

Very recently, there has been useful work on new standard samples, where the measurand is the surface yield of an implanted (amorphized) silicon sample (Lennard *et al* 1999, Bianconi *et al* 2000) This is equivalent to an absolute measurement of the energy loss of Si (see Konac *et al* (1998) and the discussion in Barradas *et al* (2002a)). In the work of Bianconi *et al* labs made absolute measurements of the charge · solid-angle product, at nominally 1% accuracy, and got agreement within the stated error. The traceability of Lennard *et al*'s work is not so easy to establish, but they obtain the same values. Niemann *et al* (1996) have also made measurements of energy loss in Si at an accuracy approaching 1%. The point here is that Bi or Sb implant samples are specific artefacts, but every lab can make their own amorphized Si samples on demand. Secondary standards must be used systematically with the Bi certified standards, with the associated error and complexity; not so for the amorphized Si. The difficulty with certifying the Bi implants has been in establishing the real variation across the implant batch, but the uniformity and purity of modern production silicon ingots has been established at extraordinary sensitivity and accuracy: modern standard RBS samples can now take advantage of this.

It should not surprise the reader, bearing in mind the preceding discussion, that much current routine RBS has

difficulty establishing an accuracy better than 10%. Critical work is usually done relative to internal standards in the sample set: the accuracy of such work is usually very difficult to trace.

Boudreault *et al* (2002) have now demonstrated an RBS analysis at an accuracy certifiable near the 1% level, traceable through the new IRMM/BAM standard samples, and which could be implemented as a routine tool. Heavy ion implants into silicon can be chosen to leave the surface implanted layer fully amorphized. Standard implants like these are important in implantation labs for validating the implanter performance. Therefore, a routine certifiable analysis is of considerable value.

Two detectors at different scattering angles are used. The DataFurnace is used to calculate the depth profile as described above: this calculation is done self-consistently using correct stopping powers (we remind the reader that most widely used codes do not do a proper self-consistent calculation, giving an error that increases with As concentration). The pileup correction of Jeynes *et al* (1997) is used. The integration of the As profile gives the As atom density directly. Clearly, such an analysis is traceable not only to the value of the stopping powers at the energy of analysis but also to the shape of the energy loss as a function of energy (although for low energy implants a single correction value is adequately accurate). The new accurate values of the energy loss function in silicon are easily included explicitly in the DataFurnace energy loss database, making a fully traceable routine analysis straightforward.

The interesting thing about this approach is that the spectra from both detectors are handled together self-consistently: this is equivalent to two essentially independent measurements of the same quantity (given the accelerator parameters of course). Not only this but also the data reduction is automatic. Thus we demonstrate a rapid routine automatic analysis of certifiable accuracy where a single measurement contains its own validation with information from two independent data channels. In the case shown, the coefficient of variation of the ratio of the doses determined for the two detectors is about 2% (for a dose of about 5.10^{15} As/cm^2), consistent with the estimate of the uncertainty of the measurements. The values are about 1% lower if infinite As dilution is assumed for the calculation of stopping power, emphasising the importance of a correct calculation. The accuracy of the electronic energy calibration (independently determined for each detector) is important, since it is comparable to the counting statistics only if carefully done. The charge · solid-angle product is determined absolutely (again, independently for each detector) from the standard value used for the energy loss.

11.2. Elastic (non-Rutherford) scattering

We have recently demonstrated a very good precision of 2% and quite a good accuracy of 10% in a determination of the C content of Ni–Ta–C magnetron-sputtered films on a silicon substrate using a mixed EBS/RBS analysis and a 1.75 MeV H beam (Jeynes *et al* 2000a). These films were very uniform and reproducible, and it was possible, assuming their uniformity, to use a transparent (and hence traceable) manual method for data reduction to obtain the stoichiometry. The difficulty with EBS is the very strongly non-Rutherford cross-section for both the C and the Si signals. Not only can the cross-section enhancement be very large (peaking at a factor of about 60 for C for a proton beam of 1.737 MeV) but the variation with energy can be equally large. The paper includes a discussion of the cross-sections, which are outside our present scope. The successful use of EBS for accurate analysis clearly depends on accurate cross-sections. However, it also depends on codes that can effectively implement these cross-sections. H EBS is hard to use with traditional data reduction methods since there is usually considerable elemental overlap even with simple samples. DataFurnace is therefore particularly valuable for extracting depth profiles from H spectra. In this case we were able to demonstrate the validity of the assumption of uniformity of the films that was made for the manual analysis. The DataFurnace and the manual analysis agreed at the analysis precision. This is not necessary: the data reduction algorithms for the two methods are independent (although of course the same energy loss values and instrumental parameters are used for both analyses). This work is an important validation of the DataFurnace code.

It is worth remarking that these data have also been successfully analysed by an artificial neural network (ANN) code (Vieira and Barradas 2001), relying on the accuracy of the DataFurnace analysis to validate the ANN methods.

11.3. Microbeam RBS

An interesting example of an accurate analysis is the recent microbeam analysis of copper containing deposits printed with an inkjet (Jeynes *et al* 2002, Rozenberg *et al* 2002): the inkspots were about 300 μm across and very non-uniform needing a beam spot size of 10 μm. Again the RBS spectra were ambiguous, with the added problem that the true collected charge had to be determined from the spectra themselves (a standard problem with the microbeam). We were able to demonstrate from the objective goodness of fit (the χ^2 function) for a range of possible inkspot compositions that the inkspots were at least 90% copper by weight.

11.4. Conclusion

Analytical accuracy depends in all cases on being able to objectively estimate the confidence interval for the results. DataFurnace is the only code that can do this reliably for the general IBA data we have been describing, using the MCMC methods we have described above (Fischer *et al*'s MaxEnt code appears to be too cumbersome for general purpose use). The simple statistics we currently use on the MCMC data are very well suited for this purpose. However, more mathematical work is required to fully validate the cooling schedule and other details of both the MCMC and the SA algorithms.

12. Forward model limitations: stopping powers

The analysis of samples like optical filters make a dramatic demonstration of the power of these new techniques. Jeynes *et al* (2000b) have described the analysis of a 21 layer anti-reflection coating consisting of a silica/zirconia stack on a glass substrate using 2.2 MeV ^{4}He RBS (figure 11). Using the proper depth dependent energy resolution function we could

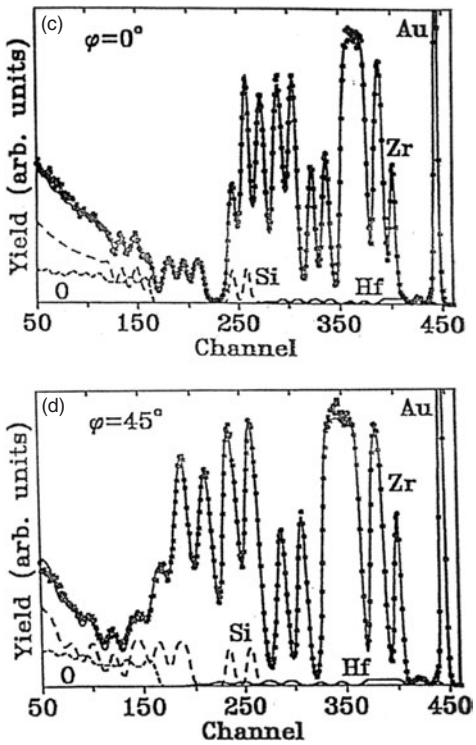

Figure 11. 2 MeV 4He$^+$ RBS data (· · · · · ·) and DataFurnace fit (——) of a 21 layer anti-reflection coating of silica and zirconia on glass. The DataFurnace fit assumes molecules (no free oxygen), where the zirconia has a Hf contamination. The energy resolution as a function of depth is calculated with the DEPTH code of Szilágyi *et al* 1995. Two angles of beam incidence are used sequentially with the data fitted simultaneously. Partial spectra for Hf, Si and O are also shown. From figure 2 of Jeynes *et al* (2000).

demonstrate a perfect self-consistent fit to double detector data (actually this data was single detector, but with two incident angles of the beam). An MCMC analysis was carried out, and deep in the stack, at a depth of a micron, we find that, for example, the 17th layer (zirconia) is 30.0 ± 2.6 nm thick, where the error has a confidence of 95%.

We should note that the MCMC information is now being treated in a different way from the simple display as in figures 8 and 10 for example. The fit was carried out allowing the zirconia and silica to mix (no solution is available if mixing is not allowed). The errors calculated by MCMC are available as a function of depth. Equivalent pure layer thicknesses are calculated, with their errors, by splitting the 'mixed' regions equally between their pure neighbours.

This analysis was carried out using the information that only zirconia and silica are present in the stack: we used three molecules, ZrO_2 (with a Hf contamination), SiO_2 and the five element float glass substrate including 0.2 at% Sn which significantly complicates the spectra. Thus although seven different elements are significant in the sample only three molecular fitting parameters are used, and the light element O is always correlated with heavier elements with larger signals. We shall see that in fact this correlation of the low and high energy parts of the spectrum is also essential to obtain a correct solution for another reason. Clearly with such a complicated sample it is very desirable to restrict the state space with as much prior information as is available.

It is astonishing that such a precision (better than 3 nm) is available so deep in such a complicated sample. For comparison, the detector energy resolution at around 12 keV is equivalent to a depth in silicon of about 30 nm. Energy straggling will rapidly degrade this with depth. Of course, the precision of the layer thickness calculation is not the same as an objective evaluation of the true depth resolution. We have already noted that many quantities can be determined at a precision much better than the nominal depth resolution. In this case, we have imposed the assumption of sharp interfaces onto the sample, and then we are effectively counting atoms per layer, something RBS is extremely good at.

The question then arises: what is the accuracy of the determination of the layer thicknesses? For thin films the answer is simple: counting atoms simply depends on the accuracy of the system calibration. However, for thick films we have to consider the effects of the enhanced backgrounds and the spectral distortions caused by multiple and plural scattering effects. Some of these effects can be largely eliminated with standard analytical methods as described above, but complex spectra like these will be very sensitive to them. This is as yet an open problem since what is needed is well founded analytical approximations for these effects that can be incorporated into SA.

If on the other hand we ask what is the confidence we have in the interface information (recall that the fit insisted on mixed interface regions) the answer is very different. We tried initially to fit these spectra with an old code that did not permit molecules. We found that solutions were very easy to find, but that they always involved no correlation between the oxygen and the metals. The elemental solutions did not give the right stoichiometries. It turns out that where there are strong interface signals SA is extremely sensitive to the system calibration. Moreover, the position of the interface signals is determined by energy loss. Therefore any error in the energy loss function of one element that is not exactly matched by corresponding errors in all the other relevant elements will make the code want to put the interface signals for the different elements in different places. Where the elemental signals are not correlated by the use of molecular parameters the real correlation between elements will be obscured by the errors in the energy loss database. Similarly, where molecular parameters are used, interface information will also be obscured. Therefore, we suspect that the insistence of the DataFurnace that the interfaces are mixed is probably an artefact due to errors in the stopping power database.

13. Future developments

13.1. Turnkey RBS

Historically the use of IBA has been largely restricted to university research groups. There has been an explosion in the development of a large variety of beautiful techniques and there is no doubt of its utility in research. However, the impact on industry of IBA methods has been marginal, and we believe that this is largely due to the time and skill required to properly interpret even RBS data, the simplest of the IBA techniques. The new data reduction methods that we have

described here are powerful enough to revolutionize IBA. In the future, turnkey benchtop accelerators will be operated by technical or graduate level staff (rather than research staff) and profiles will be generated automatically and on-line from the spectra. Staff training should take no longer than two or three days, and there will be well defined quality assurance procedures both for calibrating the instrument and presenting and validating data. Such instruments will still be limited by the skill of the operators, and research staff would be able to push the instruments much further. However, routine analysis will be available for a wide range of sample types at an accuracy certifiable at or near the 1% level, and at a fraction of the current cost. Immediately a wide range of analyses relevant to process development, production control and quality control become feasible and such simplified instruments will find widespread use.

13.2. EBS

We anticipate that the progress made recently in understanding the functional form of the EBS cross-sections (Gurbich 1997, 1998, 1999) should allow a comprehensive database for these cross-sections to be loaded, and for the distinction between RBS and EBS to be transparent to the user. At present the use of EBS is badly hampered because the analyst must make sure that the scattering angles used conform to the angle for which the cross-sections were measured, but Gurbich's formalism will allow the interpolations from the database to any angle. Moreover, the Handbook (Tesmer and Nastasi 1995) can be misleading and is not suitable for accurate work: a more reliable cross-section database is very desirable.

13.3. PIXE, VASE, NDP

So far we have not attempted to implement SA for PIXE data. PIXE and RBS are complementary: RBS frequently does not have unequivocal elemental identification and PIXE is rather insensitive to inhomogeneity in depth. The two together should be very powerful indeed. In principle the PIXE forward model should not be too hard to implement, we have not done this up to now since it is completely different physics from particle scattering. We should mention that just as PIXE could be implemented with a new forward model, so could other techniques. We have already explored the use of simulated annealing with variable angle spectroscopic ellipsometry (VASE) (Barradas *et al* 1999e): this is a widespread and powerful technique to which IBA is complementary. We believe that a DataFurnace extension that allowed simultaneous self-consistent fitting of IBA and ellipsometric data would be tremendously powerful. An extension to neutron depth profiling (NDP) has recently been implemented.

13.4. High depth resolution

High depth resolution is of great current interest, with many important technologies dependent on the manipulation of very thin films. We have demonstrated that when combined with an accurate function of energy resolution with depth a DataFurnace analysis can yield an astonishing depth resolution for the most complex sample. We believe that SA could be used as a preprocessor for a maximum entropy code, since the computation time for such a code is dramatically reduced if the position of the solution in state space is approximately known. The drawback of this approach is that the detector transfer function must be accurately known, but the benefit would be a greatly enhanced depth resolution for a reasonable computation time. A sub-atomic depth resolution should be available if high resolution detectors (e.g. Lanford *et al* (1998)) are used.

13.5. Artificial neural networks

A very interesting recent development, completely unrelated to SA, is in the demonstration that ANNs can be effective and surprisingly accurate in interpreting RBS spectra (Vieira and Barradas 2000, 2001, Barradas and Vieira 2000, Barradas *et al* 2001). It has become clear that ANNs can only be used to interpolate, not extrapolate, the training set (Vieira *et al* 2001). The interesting thing about ANNs is that in operation they are entirely model-free—the ANN is a 'black box' with a spectrum as input and the required parameters as output and there is no physics calculation in the box. The physics is all implicit in the set of spectra and their solutions used to train the ANN. Note that the calculation of the ANN is effectively instantaneous: there is no computation time to extract the programmed parameters from the spectrum. The prospect has been raised of 'RBS without humans' (Barradas *et al* 2002b), but more realistically we can consider using ANNs in special situations where large numbers of similar spectra are to be analysed.

13.6. MCMC

Because of the pressure to have on-line analysis with multiple techniques, and because of the highly computationally intensive nature of both SA and the forward models (especially when the full depth dependent energy resolution function is incorporated), algorithmic issues will remain important. We expect significant increases in speed with a more efficient generation function, and although we currently use an adaptive cooling schedule we do not believe it is anywhere near optimal. Also the currently used local minimization is slow. MCMC methods could be used for characterizing the state space of spectra more systematically: looking for the set of near-optimal solutions, which may be effectively discontinuous as in our silicides example. This may enable priors to be specified more robustly. Of course, the MCMC calculation makes vast amounts of information available, from which we only extract a variance at present. This data could be treated in a more sophisticated way.

These ideas are explored by Marriott *et al* (2002), who have found a far more efficient algorithm than the one we currently use. They look at a different MCMC algorithm which is based on ideas from the Gibbs sampling formulation of MCMC rather than the Metropolis–Hastings method (SA) described here. This new method more fully exploits the information available in the forward model calculation (the elemental sub-spectra) to efficiently generate possible new states. The better the generation function the more efficient the MCMC.

13.7. Parallel processing

MCMC (and therefore also SA) is easy to implement on parallel processor machines, and we expect that any serious increase in the industrial use of IBA techniques will also lead to very high specification hardware being used. After all, a £2K PC is only 0.2% of the cost of a £1M accelerator system.

13.8. Unresolved algorithmic issues

Unresolved algorithmic issues include some *ad hoc* parameters such as the 1.5 exponent used for normalizing the chisquared (Barradas *et al* 1999d), this means that we cannot yet demonstrate that we weight multiple spectra correctly. More important is the outstanding problem of continuity which represents important prior information about the sample that is rather hard to specify objectively. Has the sample got implant or diffusion profiles? How many layers does it have (we already estimate this from the derivative of the spectrum, but we are not convinced that an unequivocal algorithm exists)? What is the difference between a diffused interface and a diffusion profile? Progress in systematising these questions will greatly help the implementation of turnkey IBA.

13.9. Unresolved forward model problems

There are two major areas where the IBA forward model is unsatisfactory and progress in these will improve its accuracy.

Multiple and plural scattering are well simulated with Monte Carlo methods. These effects become important for thick samples and for glancing angle IBA. The contribution to straggling of multiple straggling effects is estimated well by Szilágyi's DEPTH code, but its low energy background and the spectral distortion of plural scattering cannot yet be estimated simply. Amsel *et al* (2003) have just published a systematic analytical and numerical account of multiple scattering which we believe will prove very valuable.

The energy loss database represents a huge amount of experimental and theoretical work, but its accuracy is still rather poor in general. We believe that with accurate data analysis for IBA now being available it may be possible to find much more rapid ways to obtain high quality energy loss data. In any case, an accurate knowledge of the energy loss is essential for accurate IBA.

14. Summary

Since the analysis of RBS spectra using SA methods was first published in April 1997 we have generalized the method to all the depth profiling (particle scattering) IBA techniques, and also supplied a highly usable interface for the analyst. We have called this the IBA DataFurnace. We have here reviewed the literature both on these developments and on their context.

There are a very wide range of powerful IBA techniques in use in the scientific community. 'Simple' depth profiling may be the least interesting of these techniques, but it is very widely applicable by thin film technologists and materials scientists, and we have produced a code which takes the drudgery out of it.

Depth profiling by IBA using the IBA DataFurnace to automatically fit the spectra is a qualitative advance on previous methods of extracting profiles by IBA, and amounts to a new and very powerful tool for depth profiling thin film samples.

Acknowledgments

This work was supported by the Surrey IBC under EPSRC contracts GRJ 97540, GRK56247 and GRL 78512. MJ was supported by EPSRC and by the National University of Singapore (grantholders PKM and F Watts). We are grateful to Prof. B J Sealy for his encouragement and to Alex Gurbich for a careful and critical reading of a draft of the manuscript. We would also like to thank Chris Burt for skilfully operating the accelerator.

References

Aarts E and Korst J 1989 Simulated annealing and Boltzmann machines: a stochastic approach to combinatorial optimization and neural computing (Chichester: Wiley)

Alkemade P F A, Habraken F H P M and van der Weg W F 1990 On the ambiguity in the analysis of Rutherford backscattering spectra *Nucl. Instrum. Methods* B **45** 139–42

Almeida S A, Silva S R P, Sealy B J and Watts J F 1999 Bond formation in ion beam synthesised amorphous gallium nitride *Thin Solid Films* **343–344** 632–6

Alves E, Barradas N P, Monteiro T, Correia R and Kreissig U 2002 Ion beam studies of MBE grown GaN films on (111) silicon substrates *Nucl. Instrum. Methods* B **188** 73–7

Amsel G, Menu M, Moulin J and Salomon J 1990 The 2 MV tandem pelletron accelerator of the Louvre Museum *Nucl. Instrum. Methods* B **45** 296–301

Amsel G 1996 CUTBA—cleaning up the tower of babel of acronyms in IBA *Nucl. Instrum. Methods* B **118** 52–6

Amsel G, Battistig G and L'Hoir A 2003 Small angle multiple scattering of fast ions, physics, stochastic theory and numerical calculations *Nucl. Instrum. Methods* B **201** 325–88

Baker M A, Greaves S J, Wendler E and Fox V 2000 A comparison of *in situ* polishing and ion beam sputtering as surface preparation methods for XPS analysis of PVD coatings *Thin Solid Films* **277–278** 473–7

Barradas N P, Soares J C, da Silva M F, Pászti F and Szilágyi E 1994 Study of multilayer substrate roughness using RBS with improved depth resolution *Nucl. Instrum. Methods* B **94** 266–70

Barradas N P, Jeynes C and Webb R P 1997 Simulated annealing analysis of Rutherford backscattering data *Appl. Phys. Lett.* **71** 291–3

Barradas N P, Jeynes C and Harry M A 1998a RBS/simulated annealing analysis of iron-cobalt silicides *Nucl. Instrum. Methods* B **136–138** 1163–7

Barradas N P, Jeynes C, Homewood K P, Sealy B J and Milosavljević M 1998b RBS/simulated annealing analysis of silicide formation in Fe/Si systems *Nucl. Instrum. Methods* B **139** 235–8

Barradas N P, Jeynes C and Jackson S M 1998c RBS/simulated annealing analysis of buried $SiCO_x$ layers formed by ion implantation of O into cubic silicon carbide *Nucl. Instrum. Methods* B **136–138** 1168–71

Barradas N P, Jeynes C, Mironov O A, Phillipps P J and Parker E H C 1998d High depth resolution Rutherford backscattering analysis of Si–$Si_{0.78}Ge_{0.22}$/(001)Si superlattices *Nucl. Instrum. Methods* B **139** 239

Barradas N P, Marriott P K, Jeynes C and Webb R P 1998e The RBS datafurnace: simulated annealing *Nucl. Instrum. Methods* B **136–138** 1157–62

Barradas N P, Almeida S A, Jeynes C, Knights A P, Silva S R P and Sealy B J 1999a RBS and ERDA simulated annealing study of ion beam synthesised gallium nitride *Nucl. Instrum. Methods* B **148** 463–7

Barradas N P, Jeynes C, Jenkin M and Marriott P K 1999b Bayesian error analysis of Rutherford backscattering spectra *Thin Solid Films* **343–344** 31–4

Barradas N P, Jeynes C, Kusano Y, Evetts J E and Hutchings I M 1999c RBS/simulated annealing and FTIR characterisation of BCN films deposited by dual magnetron sputtering *Applications of Accelerators in Research and Industry* CP475 ed J L Duggan and I L Morgan (New York: AIP) pp 504–7

Barradas N P, Jeynes C, Webb R P, Kreissig U and Grötzschel R 1999d Unambiguous automatic evaluation of multiple ion beam analysis data with simulated annealing *Nucl. Instrum. Methods* B **149** 233–7

Barradas N P, Keddie J L and Sackin R 1999e Bayesian inference analysis of ellipsometry data *Phys. Rev.* E **59** 6138–51

Barradas N P, Knights A P, Jeynes C, Mironov O A, Grasby T J and Parker E H C 1999f High-depth-resolution RBS data and error analysis of SiGe systems using the simulated annealing and Markov Chain Monte Carlo algorithms *Phys. Rev.* B **59** 5097–105

Barradas N P and Smith R 1999g Simulated annealing analysis of nuclear reaction analysis measurements of polystyrene systems *J. Phys.* D **32** 2964–71

Barradas N P, Webb R P and Jeynes C 1999h WiNDF: a windows interface to the DataFurnace code for analysing IBA data *Presented at IBA14 (Dresden, July 1999)* Text available on www.ee.surrey.ac.uk/SCRIBA/ndf

Barradas N P, Khan R U A, Anguita J V, Silva S R P, Kreissig U, Grötzschel R and Möller W 2000a *Nucl. Instrum. Methods* B **161** 969–74

Barradas N P, Parascandola S, Sealy B J, Grötzschel R and Kreissig U 2000b Simultaneous and consistent analysis of NRA, RBS and ERDA data with the IBA DataFurnace *Nucl. Instrum. Methods* B **161–163** 308–13

Barradas N P and Vieira A 2000c Artificial neural network algorithm for analysis of Rutherford backscattering data *Phys. Rev.* E **62** 5818–29

Barradas N P 2001a Rutherford backscattering analysis of thin films and superlattices with roughness *J. Phys.* D **34** 2109–16

Barradas N P, Sequeira A D, Franco N, Myronov M, Mironov O A, Philips P J and Parker E H C 2001b RBS analysis of MBE grown SiGe/(001)Si heterostructures with thin high Ge content SiGe channels for HMOS transistors *Mod. Phys. Lett.* B **15** 1297–304

Barradas N P 2002a Fitting of RBS data including roughness: application to Co/Re multilayers *Nucl. Instrum. Methods* B **190** 247–51

Barradas N P, Jeynes C, Webb R P and Wendler E 2002b Accurate determination of the stopping power of ^{4}He in Si using Bayesian inference *Nucl. Instrum. Methods* B **194** 15–25

Barradas N P, Patrício R and Vieira A 2002c RBS without humans IBA15 *Nucl. Instrum. Methods* B **190** 231–6

Bauer P, Steinbauer E and Biersack J P 1992 The width of an RBS spectrum: influence of plural and multiple scattering *Nucl. Instrum. Methods* B **64** 711–5

Bauer P, Steinbauer E and Biersack J P 1993 RBS beyond the single scattering model *Nucl. Instrum. Methods* B **79** 443–5

Bayes R T 1763 Essay toward solving a problem in the doctrine of chance *Phil. Trans. R. Soc.* **53** 370

Belson A *et al* 1999 Ion beam synthesised $FeSi_2$— development of band gap and structure during annealing *CREST Masterclass Project: Presented at ESPRIT Advanced Research Initiative in Microelectronics (MEL-ARI) (Athens, October 1999)*

Bettiol A A, Jamieson D N, Prawer S and Allen M G 1994 Ion beam induced luminescence from diamond and other crystals from a nuclear microbeam *Nucl. Instrum. Methods* B **85** 775–9

Bianconi M *et al* 2000 The Si surface yield as a calibration standard for RBS *Nucl. Instrum. Methods* B **161–163** 293–6

Bibic N, Dhar S, Milosavljević M, Removic K, Rissanen L and Lieb K P 2000 Interface mixing in Ta/Si bilayers with Ar ions *Nucl. Instrum. Methods* B **161–163** 1011–5

Blaauw M, Campbell J L, Fazinić S, Jakšić M, Orlic I and Van Espen P 2002 The 2000 IAEA intercomparison of PIXE spectrum analysis software *Nucl. Instrum. Methods* B **189** 113–22

Børgesen P, Behrisch R and Scherzer B M U 1982 Depth profiling by ion-beam spectrometry *Appl. Phys.* A **27** 183–95

Boudreault G, Jeynes C, Wendler E, Nejim A, Webb R P and Wätjen U 2002 Accurate RBS measurement of ion implant doses in silicon *Surf. Interface Anal.* **33** 478–86

Bragg W H and Kleeman R 1905 On the α particles of radium, and their loss of range in passing through various atoms and molecules *Phil. Mag.* **10** S318–40

Breese M B H, Amaku A and Wilshaw P R 1998a A comparison between the use of EBIC and IBIC microscopy for semiconductor defect analysis *Nucl. Instrum. Methods* B **136–138** 1355–60

Breese M B H, King P J C and de Kerckhove D G 1998b Strain and defect imaging using a nuclear microprobe *Nucl. Instrum. Methods* B **136–138** 23–34

Brice D K 1973 Theoretical analysis of the energy spectra of backscattered ions *Thin Solid Films* **19** 121–35

Butler J W 1990 Criteria for validity of Rutherford scatter analysis *Nucl. Instrum. Methods* B **45** 160–5

Cappellani A, Keddie J L, Barradas N P and Jackson S M 1999 Processing and characterisation of sol-gel deposited Ta_2O_5 and TiO_2–Ta_2O_5 dielectric thin films *Solid State Electron.* **43** 1095–9

Carey J D, Forrest R D, Khan R U A and Silva R R P 2000 Influence of sp(2) clusters on the field emission properties of amorphous carbon thin films *Appl. Phys. Lett.* **77** 2006–8

Carey J D and Silva R R P 2001 Conditioning of hydrogenated amorphous carbon thin films for field emission via current stressing *Appl. Phys. Lett.* **78** 347–9

Chu W K, Mayer J W and Nicolet M-A 1978 *Backscattering Spectrometry* (New York: Academic)

Cumpson P J 1995 Angle-resolved XPS and AES: depth resolution limits and a general comparison of properties of depth-profile reconstruction methods *J. Elec. Spec. Relat. Methods* **73** 25–52

Dhar S, Milosavljević M, Bibić N and Lieb K P 2002 Atomic mixing and interface reactions in Ta/Si bilayers during noble-gas ion irradiation *Phys. Rev.* B **65** Art. no 024109

Doolittle L R 1986 A semi-automatic algorithm for RBS analyis *Nucl. Instrum. Methods* B **15** 227–31

Ecker K H, Wätjen U, Berger A, Persson L, Pritzkow W, Radtke M and Riesemeier H 2002 RBS, SY-XRF, INAA and ICP-IDMS of antimony implanted in silicon—a multi-method approach to characterize and certify a reference material *Nucl. Instrum. Methods* B **188** 120–5

Eckstein W and Mayer M 1999 Rutherford backscattering from layered structures beyond the single scattering model *Nucl. Instrum. Methods* B **153** 337–44

Edge R D 1983 RBS microscopic Tomography *IEEE Trans. Nucl. Sci.* **NS-30** 1685–7

Edge R D 1988 Element distributions at depth from an iterative analysis of RBS spectra *Nucl. Instrum. Methods* B **35** 309–14

Feldman L C, Mayer J W and Picraux S T 1982 *Materials Analysis by Ion Channeling* (New York: Academic)

Fischer R, Mayer M, von der Linden W and Dose V 1997 Enhancement of the energy resolution in ion-beam experiments with the maximum-entropy method *Phys. Rev.* E **55** 6667–3

Fischer R, Mayer M, von der Linden W and Dose V 1998 Energy resolution enhancement in ion beam experiments with Bayesian probability theory *Nucl. Instrum. Methods* B **136–138** 1140–5

Fitz T and Möller W 2002 AlN growth kinetics during ion nitriding of aluminum *J. Appl. Phys.* **92** 6862–7

Garrett A 1991 Ockham's Razor *Phys. World* **4** 39–42

Geiger H and Marsden E 1909 On a diffuse reflection of the α-particles *R. Soc. Proc.* A **82** 495–500

Geiger H 1910 The scattering of the α-particles by matter *R. Soc. Proc.* A **83** 492–504

Geiger H and Marsden E 1913 On the laws of deflexion of α-particles through large angles *Phil. Mag.* **25** 604–23

Geman S and Geman D 1984 Stochastic relaxation, Gibbs distributions and the Bayesian restoration of images *IEEE Trans. Pattern Anal. Mach. Intell.* **6** 721–41
Gilks W R and Richardson S (ed) 1996 *Markov Chain Monte Carlo* (London: Chapman and Hall)
Grime G W and Dawson M D 1995 Recent developments in data acquisition and processing on the Oxford scanning proton microprobe *Nucl. Instrum. Methods* B **104** 107–13
Götz G and Gärtner K (ed) 1988 *High Energy Ion Beam Analysis of Solids* (Berlin: Akademie-Verlag)
Gurbich A F 1995 On the origin of the low energy tail in charged particle spectra *Nucl. Instrum. Methods* A **364** 496–500
Gurbich A F 1997 Evaluation of non-Rutherford proton elastic scattering cross-section for oxygen *Nucl. Instrum. Methods* B **129** 311–6
Gurbich A F 1998 Evaluation of non-Rutherford proton elastic scattering cross-section for carbon *Nucl. Instrum. Methods* B **136–138** 60–5
Gurbich A F 1998 Evaluation of non-Rutherford proton elastic scattering cross-section for silicon *Nucl. Instrum. Methods* B **145** 578–83
Gurbich A F 1999 Proton elastic scattering cross-section for carbon: confrontation of theory and experiment *Nucl. Instrum. Methods* B **152** 403–5
Gurbich A F, Barradas N P, Jeynes C and Wendler E 2002 Applying elastic backscattering spectrometry when the nuclear excitation function has a fine structure *Nucl. Instrum. Methods* B **190** 237–40
Harbsmeier F, Bolse W and Flank A-M 2000 Solid state reaction in Si–C multilayers induced by ion bombardment *Nucl. Instrum. Methods* B **166–167** 385–9
Harry M A, Curello G, Finney M S, Reeson K J and Sealy B J 1996 Structural properties of ion beam synthesised iron–cobalt silicides *J. Phys.* D **29** 1822–30
Hirvonen J-P 1995 Nuclear reaction analysis: particle-gamma reactions *Handbook* ed Tesmer and Nastasi, chapter 7
Jackson S M 1998 Optical characterisation of cubic silicon carbide *PhD Thesis* University of Surrey
Jeynes C, Jafri Z H, Webb R P, Ashwin M J and Kimber A C 1997 Accurate RBS measurements of the in content of InGaAs thin films *Surf. Interface Anal.* **25** 254–60
Jeynes C, Barradas N P, Blewett M J and Webb R P 1998 Improved ion beam analysis facilities at the University of Surrey *Nucl. Instrum. Methods* B **136–138** 1229–34
Jeynes C, Barradas N P, Wilde J R and Greer A L 2000a Composition of TaNiC thick films using SimAnn: elastic backscattering spectrometry *Nucl. Instrum. Methods* B **161–163** 287–92
Jeynes C, Barradas N P, Rafla-Yuan H, Hichwa B P and Close R 2000b Accurate depth profiling of complex optical coatings *Surf. Interface Anal.* **30** 237–42
Jeynes C, Rozenburg G G, Speakman S P and Steinke J H G 2002 A microbeam RBS analysis of low temperature direct-write inkjet deposited copper *Nucl. Instrum. Methods* B **188** 141–5
Johanssen S A E and Campbell J L 1988 *PIXE: A Novel Technique for Elemental Analysis* (Chichester: Wiley)
Kirkpatrick S, Gelatt C D Jr and Vecchi M P 1983 Optimization by simulated annealing *Science* **220** 671–80
Konac G, Kalbitzer S, Klatt C, Niemann D and Stoll R 1998 Energy loss and straggling of H and He ions of keV energies in Si and C *Nucl. Instrum. Methods* B **136–138** 159–65
Kótai E 1994 Computer methods for analysis and simulation of RBS and ERDA spectra *Nucl. Instrum. Methods* B **85** 588–96
Kogan D L, Kazancev A M and Kuzmin L E 1994 BEAM EXPERT—integrated software for nuclear analysis *Nucl. Instrum. Methods* B **88** 495–8
Lanford W A, Anderberg B, Enge H and Hjorvarsson B 1998 Compact broad range magnetic spectrometer for use in ion beam analysis *Nucl. Instrum. Methods* B **136–138** 1177–82
Lee P M 1977 *Bayesian Statistics: An Introduction* 2nd edn (London: Arnold)
Lennard W N, Tong S Y, Massoumi G R and Wong L 1990 On the calibration of low energy ion accelerators *Nucl. Instrum. Methods* B **45** 281–84
Lennard W N, Massoumi G R, Alkemade P F A, Mitchell I V, McIntyre N S and Davison R D 1993 Deuterium depth distribution investigations in Zr and ZrO_2 *Nucl. Instrum. Methods* B **73** 203–13
Lennard W N, Massoumi G R, Simpson T W and Mitchell I V 1999 Improved stoichiometry measurements using ^{4}He backscattering: experiment and simulation *Nucl. Instrum. Methods* B **152** 370–6
Lennard W N 2000 Private communication
Leong D, Harry M A, Reeson K J and Homewood K P 1997 A silicon/iron disilicide light emitting diode operating at a wavelength of 1.5 μm *Nature* **387** 686–8
Liew S C, Loh K K and Tang S M 1994 Application of an iterative maximum-likelihood algorithm in PIXE depth profiling of trace elements *Nucl. Instrum. Methods* B **85** 621–6
Loh K K, Sow C H, Tan K H, Tan H S, Tang S M, Orlic I and Osipowitz T 1993 Measurement of phosphorus content in silica layers *Nucl. Instrum. Methods* B **75** 364–6
Malmqvist K G (ed) 1999 *Proc. 8th Int. Conf. on Particle Induced X-ray Emission and its Applications (Lund, 14–18 June 1998) Nucl. Instrum. Methods* B **150**
Mallégol J, Gorse J-P, Jeynes C, Dupont O and Keddie J 2002 Origins and effects of a surfactant excess at the surface of waterborne acrylic pressure sensitive adhesives *Langmiur* **18** 4478–87
Marin N, Serruys Y and Calmon P 1996 Extraction of lateral non-uniformity statistics from Rutherford backscattering spectra *Nucl. Instrum. Methods* B **108** 179–87
Marriott P K, Jenkin M, Jeynes C, Barradas N P, Webb R P and Sealy B J 1999 Rapid accurate automated analysis of complex ion beam analysis data *Applications of Accelerators in Research and Industry* vol CP475, ed J L Duggan and I L Morgan (New York: AIP) pp 592–5
Marriott P K, Jenkin M and Jeynes C 2002 The Bayesian analysis of Rutherford backscatter spectra Proc. Int. Conf. on Computational Mathematics and Modeling *East-West J. Math.* p 15
Metropolis N, Rosenbluth A W, Rosenbluth M N, Teller A H and Teller E 1953 Equation of state calculations by fast computing machines *J. Chem. Phys.* **21** 1087–92
Mayer J W and Ziegler J F (ed) 1973 *Proc. Int. Conf. on Ion Beam Surface Layer Analysis, Thin Solid Films* **19**
Mayer J W and Rimini E (ed) 1977 *Ion Beam Handbook for Materials Analysis* (New York: Academic) Known as the 'Catania' Handbook, it includes a section on PIXE
Mayer M 1997 SIMNRA user's guide *Technical Report* IPP 9/113, Max-Planck-Institut für Plasmaphysik, Garching, Germany
Milosavljević M, Bibic N, Perusko D, Jeynes C and Bangert U 2000 The effects of implanted arsenic on titanium silicide formation *Special Defects in Semiconducting Materials* ed R P Agarwala *Solid State Phenomena* **71** 142–172 (Scitech Publications, Switzerland, 1999)
Milosavljević M, Shao G, Bibić N, McKinty C N, Jeynes C and Homewood K P 2001 Amorphous-iron disilicide: a promising semiconductor *Appl. Phys. Lett.* **79** 1438–40
Milosavljević M, Shao G, Bibić N, McKinty C N, Jeynes C and Homewood K P 2002 Synthesis of amorphous $FeSi_2$ by ion beam mixing *Nucl. Instrum. Methods* B **188** 166–9
Möller W *et al* (ed) 2000 *Proc. 14th Int. Conf. on Ion Beam Analysis (Dresden, September 1999) Nucl. Instrum. Methods* B **161–163**
Nagel R and Balogh A G 1999 Atomic transport in metal/ceramic interfaces under heavy ion irradiation *Nucl. Instrum. Methods* B **156** 135–42
Nagel R, Hahn H and Balogh A G 1999 Diffusion processes in metal/ceramic interfaces under heavy ion irradiation *Nucl. Instrum. Methods* B **148** 930–5

Niemann D, Konac G and Kalbitzer S 1996 Stopping power measurements of ^{1}H, ^{4}He, and ^{14}N in the energy range of 0.02–1 MeV amu^{-1} *Nucl. Instrum. Methods* B **118** 11–18

Niwa H, Nakao S and Saitoh K 1998 Application of HI-RBS to compositional analysis of thin films *Nucl. Instrum. Methods* B **136–138** 297–300

Padayachee J, Prozesky V M, von der Linden W, Nkwinika M S and Dose V 1999 Bayesian PIXE background subtraction *NIM* B **150** 129–35

Payne R S, Clough A S, Murphy P and Mills P J 1989 Use of the D(^{3}He,p)^{4}He reaction to study polymer diffusion in polymer melts *Nucl. Instrum. Methods* B **42** 130–4

Press W H, Teukolsky S A, Vetterling W T and Flannery B P 1992 *Numerical Recipes in Fortran* 2nd edn (Cambridge: Cambridge University Press) p 438

Pritzkow W, Vogl J, Berger A, Ecker K, Grötzschel R, Klingbeil P, Persson L, Riebe G and Wätjen U 2001 Contribution of ICP-IDMS to the certification of antimony implanted in a silicon wafer—comparison with RBS and INAA results *Fresenius J. Anal. Chem.* **371** 867–73

Prozesky V M, Padayachee J, Fischer R, von der Linden W, Dose V and Ryan C G 1997 The use of maximum entropy and Bayesian techniques in nuclear microprobe applications *Nucl. Instrum. Methods* B **130** 113–7

Prozesky V M, Padayachee v, Fischer R, von der Linden W, Dose V and Weller R A 1999 Bayesian techniques and the principle of maximum entropy in ion beam analysis applications *Nucl. Instrum. Methods* B **136–138** 1146–51

Prozesky V M, Przybylowicz W J and Pineda C A (ed) 1999 *Proc. 6th Int. Conf. on Nuclear Microprobe Technology and its Applications (Cape Town, 11–16 October 1998) Nucl. Instrum. Methods* B **158**

Pyt'ev Yu P 1983 Reduction problems in experimental investigations *Math. USSR-Sbornik* **120** *(Trans. 1984 Math. USSR Sbornik* **48** 237–72 (in Russia)) 237–72

Rauhala E 1995 Energy loss *IBA Handbook* ed Tesmer and Nastasi q.v. chapter 2

Respaldiza M A and Gómez-Camacho J (ed) 1997 *Applications of Ion Beam Analysis to Arts and Archaeometry* Universidad de Sevilla

Riley L S, Hall S, Harris J, Fernandez J, Gallas B, Evans A G R, Clarke J F, Humphrey J, Murray R T and Jeynes C 1999 SiGe nMOSFETs with gate oxide grown by low temperature plasma oxidation *Microelectron. Engng.* **48** 227–30

Rodil S, Morrison N A, Milne W I, Robertson J, Stolojan V and Jayawardane D N 2000 Deposition of carbon nitride films using an electron cyclotron wave resonance plasma source *Diamond Relat. Mater.* **9** 524–9

Rokita E, Maj B, Mutsaers P H A and de Voigt M J A 1997 The use of the maximum entropy method for the improvement of the spacial resolution of micro-PIXE maps *Nucl. Instrum. Methods* B **130** 138–43

Ronning C, Buttner M, Vetter U, Feldermann H, Wondratschek O, Hofsass H, Brunner W, Au F C K, Li Q and Lee S T 2001 Ion beam deposition of fluorinated amorphous carbon *J. Appl. Phys.* **90** 4237–45

Rozenberg G G, Bresler E, Speakman S P, Jeynes C and Steinke J H G 2002 Patterned low temperature copper-rich deposits using inkjet printing *Appl. Phys. Lett.* **81** 5249–51

Ross J, Barradas N P, Hill M P, Jeynes C, Morrisey P and Watts J F 2001 Rutherford backscattering spectrometry and computer simulation for the in-depth analysis of chemically modified poly(vinylidene fluoride) *J. Mater. Sci.* **36** 1–8

Rutherford E 1911 The scattering of α and β particles by matter and the structure of the atom *Phil. Mag.* **21** 669–88

Ryan C G, van Achterbergh E, Yeats C J, Drieberg S L, Mark G, McInnes B M, Win T T, Cripps G and Suter G F 2002 Quantitative, high sensitivity, high resolution, nuclear microprobe imaging of fluids, melts and minerals *Nucl. Instrum. Methods* B **188** 18–27

Seah M P, David D, Davies J A, Jeynes C, Ortega C, Sofield C and Weber G 1988 An inter-comparison of absolute measurements of the oxygen and tantalum thickness of Ta_2O_5 reference materials BCR 261 by six laboratories *Nucl. Instrum. Methods* B **30** 140–51

Serruys Y 1990 Rational smoothing applied to Rutherford backscattering spectrometry *Nucl. Instrum. Methods* B **44** 473–8

Serruys Y 1991 Simulation of Rutherford backscattering spectra: retrograde method *Nucl. Instrum. Methods* B **61** 221–5

Serruys Y, Tirara J and Calmon P 1993 Concentration profile reconstitution from Rutherford backscattering spectra *Nucl. Instrum. Methods* B **74** 565–72

Shorin V S and Sosnin A N 1992 RBS spectra for thin films with surface roughness *Nucl. Instrum. Methods* B **72** 452–6

Simon A, Pászti F, Uzonyi I, Manuaba A, KissÁ Z and Rajta I 1998 Observation of surface topography using an RBS microbeam *Nucl. Instrum. Methods* B **136–138** 344–9

Slotte J, Laakso A, Ahlgren T, Rauhala E, Salonen R, Räisänen J, Simon A, Uzonyi I, Kiss Á Z and Somorjai E 2000 Influence of surface topography on depth profiles obtained by Rutherford backscattering spectrometry *J. Appl. Phys.* **87** 140–3

Sorkin G B 1991 Efficient simulated annealing on fractal energy landscapes *Algorithmica* **6** 367–418

Stepanov A L, Hole D E and Townsend P D 1999 Reflectance of the dielectric layers containing metal nanoparticles for by ion implantation *J. Non-Cryst. Solids* **244** 275–9

Stepanov A L, Hole D E and Bukharaev A A 2001a Interaction of high-power excimer-laser pulses with soda-lime silicate glass containing ion-implanted metal nanoparticles *Vacuum* **64** 169–77

Stepanov A L, Popok V N, Hole D E and Bukharaev A A 2001b Interaction of high-power laser pulses with glasses containing implanted metallic nanoparticles *Phys. Solid State* **43** 2192–8

Stoquert J P and Szorenyi T 2002 Determination of the number and size of inhomogeneities in thin films by ion beam analysis *Phys. Rev.* B **66** 144108

Szilágyi E and Pászti F 1994 Theoretical calculation of the depth resolution of IBA methods *Nucl. Instrum. Methods* B **85** 616–20

Szilágyi E, Pászti F and Amsel G 1995 Theoretical approximations for depth resolution calculations in IBA methods *Nucl. Instrum. Methods* B **100** 103–21

Tavares C J, Rebouta L, Alves E, Barradas N P, Pacaud J and Riviére J P 2002 Study of roughness in TiAlN/Mo multilayer structures *Nucl. Instrum. Methods* B **188** 90–5

Telbizova T, Chevolleau T and Möller W 2001a Nitrogen incorporation and loss during ion nitriding of Al *Nucl. Instrum. Methods* B **184** 347–53

Telbizova T, Parascandola S, Prokert F, Barradas N P, Richter E and Möller W 2001b Ion nitriding of Al: growth kinetics and characterisation of the nitride layer *Surf. Coatings Technol.* **142** 1028–33

Tesmer J R and Nastasi M (ed) 1995 *Handbook of Modern Ion Beam Analysis* (Pittsburgh: Materials Research Society) Does not include PIXE (see Mayer and Rimini)

Tzitzinou A, Jenneson P M, Clough A S, Keddie J L, Lu J R, Zhdan P, Treacher K E and Satgaru R 1999 Surfactant concentration and morphology at the surfaces of acrylic latex films *Prog. Org. Coatings* **35** 89–99

Tirara J, Serruys Y and Trocellier P 1996 *Forward Recoil Spectrometry* (New York: Plenum)

Toal S J, Reehal H S, Webb S J, Barradas N P and Jeynes C 1999 Structural analysis of nanocrystalline SiC thin films grown on Si by ECR plasma CVD *Appl. Surface Sci.* **138–139** 424–8

Uchikoga S, Lai D F, Robertson J, Milne W I, Hatzopoulos N, Yankov R A and Weiler M 1999 Low-temperature anodic oxidation of silicon using a wave resonance plasma source *Appl. Phys. Lett.* **75** 725–7

Veloso A, Freitas P P, Wei P, Barradas N P, Soares J C, Almeida B and Sousa J B 2000 Magnetoresistance enhancement in specular, bottom-pinned, $Mn_{83}Ir_{17}$ spin valves with nano-oxide layers *Appl. Phys. Lett.* **77** 1020–2

Vieira A and Barradas N P 2000 Neural network analysis of Rutherford backscattering data *Nucl. Instrum. Methods* B **170** 235–8

Vieira A and Barradas N P 2001 Composition of NiTaC films on Si using neural networks analysis of elastic backscattering data *Nucl. Instrum. Methods* B **174** 367–72

Vieira A, Barradas N P and Jeynes C 2001 Error performance analysis of artificial neural networks applied to Rutherford backscattering data *Surf. Interface Anal.* **31** 35–8

Vizkelethy G 1995 *Nuclear Reaction Analysis: Particle–Particle Reactions* ed Tesmer and Nastasi, chapter 6

Vonsovici A, Reed G T, Evans A G R and Namavar F 1999 Loss measurements for β-SiC-on-insulator for high-speed silicon-based photonic devices *SPIE Conf. on Si-based Optoelectronics (San Jose, California, January 1999) SPIE* vol 3630, pp 115–24

Vredenberg A M, Polman A, Stolk P A, Snoeks E and Brongersma M L (ed) 1999 *Proc. 11th Int. Conf. on Ion Beam Modification of Materials (Amsterdam, August 31–September 4, 1998) Nucl. Instrum. Methods* B **148**

Watt F and Grime G W 1987 *Principles and Applications of High-Energy Ion Microbeams* (Bristol: Adam Hilger)

Wilks Y A, Slator B M and Guthrie L M 1996 *Electric Words: Dictionaries, Computers, Meanings* (Cambridge MA: MIT Press)

Williams J S and Möller W 1978 On the determination of optimum depth-resolution conditions for Rutherford backscattering analysis *Nucl. Instrum. Methods* **157** 213–21

Wagner S, Carpene E, Schaaf P and Weisheit M 2002 Formation of beta-$FeSi_2$ by excimer laser irradiation of Fe-57/Si bilayers *Appl. Surf. Sci.* **186** 156–61

Wätjen U, Bax H and Rietveld P 1992 Evaporated and implanted reference layers for calibration in surface analysis *Surf. Interface Anal.* **19** 253–8

Wätjen U and Bax H 1994 Bi-implanted silicon reference material revisited: uniformity of the remaining batch *Nucl. Instrum. Methods* B **85** 627–32

Way A S, Jeynes C and Webb R P 1999 Measurement of lateral stress in argon implanted thin gold films using quartz resonator techniques *Nucl. Instrum. Methods* B **148** 238–41

Wendler E, Jeynes C, Webb R P, Barradas N P, Thompson R and Smith R 1999 Hydrogen isotope profiling of functionalised polystyrene blends using RBS/ERD and RBS/NRA with simulated annealing analysis *11th AINSE Conf. Nuclear Techniques of Analysis, Lucas Heights, (Australia, 24–26 November 1999)*

Xie Z, Luo E Z, Peng H B, Zhao B R, Hu G D, Wilson I H, Xu J B and Zhao L H 1999 Studies of leakage current inhomogeneity of Pb(Zr, Ti)O_3/$YBa_2Cu_3O_x$ heterostructures on a nanometer scale *J. Non-Cryst. Solids* **254** 112–7

Yang C, Homman N P-O, Johanssen L and Malmqvist K G 1994 Microcharacterizing zircon mineral grain by ionoluminescence combined with PIXE *Nucl. Instrum. Methods* B **85** 808–14

Young W T, Silva S R P, Anguita J V, Shannon J M, Homewood K P and Sealy B J 2000 Low temperature growth of gallium nitride *Diamond Relat. Mater.* **9** 456–9

Yesil I M, Assmann W, Huber H and Löbner K E G 1998 Simulation of surface roughness effects in ERDA *Nucl. Instrum. Methods* B **136–138** 623–7

Ziegler J F, Biersack J P and Littmark U 1985 *The Stopping and Ranges of Ions in Solids* (New York: Pergamon)

Zhang Z, Cardoso S, Freitas P P, Wei P, Barradas N (sic), Soares J C 2001 Annealing effect of magnetic tunnel junctions with one FeO_x layer inserted at the Al_2O_3/CoFe interface *Appl. Phys. Lett.* **78** 2911–3

Zinin P, Manghnani M H, Zhang X, Feldermann H, Ronning C and Hofsass H 2002 Surface Brillouin scattering of cubic boron nitride films *J. Appl. Phys.* **91** 4196–204